Supplementary information for "Insulator-free topological photonic multi-lane highways"

Xiaohan Cui [1,2,7,*] Ruo-Yang Zhang [3,7,†] Mudi Wang [4], Zi-Xuan Gao [5], Xiao-Dong Chen [5], Zhao-Qing Zhang [2], Yun Lai [3], and C. T. Chan [2,6‡]

[1] *State Key Laboratory of Millimeter Wave and School of Information Science and Engineering, Southeast University, Nanjing, China*

[2] *Department of Physics and State Key Laboratory of Optical Quantum Materials, The Hong Kong University of Science and Technology, Hong Kong, China*

[3] *National Laboratory of Solid State Microstructures, School of Physics, Collaborative Innovation Center of Advanced Microstructures, Nanjing University, Nanjing 210093, China*

[4] *Key Laboratory of Artificial Micro- and Nanostructures of Ministry of Education and School of Physics and Technology, Wuhan University, Wuhan, China*

[5] *School of Physics & State Key Laboratory of Optoelectronic Materials and Technologies, Sun Yat-sen University, Guangzhou 510275, China.*

[6] *Institute for Advanced Study, The Hong Kong University of Science and Technology, Hong Kong, China*

[7] *These authors contributed equally: Xiaohan Cui, Ruo-Yang Zhang.*

Contents

* e-mail: cuixiaohan@seu.edu.cn

† e-mail: zhangruoyang@nju.edu.cn

‡ e-mail: phchan@ust.hk

S1. Effects of $\mathcal{P}$- and $\mathcal{T}$- breaking strength on topological photonic highway realization

A. Realization of type-A critical photonic crystal by tuning $\mathcal{T}$-breaking strength.

The experimental realization of ABCD-configured waveguides requires implementing a type-A critical photonic crystal with precisely balanced $\mathcal{P}$- and $\mathcal{T}$-breaking strengths. We achieve this by maintaining a constant external magnetic field of H_{ext} = 1100 Oe while controlling the $\mathcal{P}$-breaking strength through radius difference δd. Numerical simulations (Fig.S1) indicate that balanced symmetry breaking is achieved with d_1 = 3mm and d_2 = 3.7mm.

B. Topological photonic highways deviating from exact $\mathcal{P}$- and $\mathcal{T}$- breaking balance

While achieving PVHSM requires a precise balance between $\mathcal{P}$- and $\mathcal{T}$-breaking strength, the domain-selective unidirectional transport persists even with slight deviations in their relative strengths. Figure S2 presents our numerical simulation results. We maintained a fixed external magnetic field while varying $\mathcal{P}$-breaking strength near the phase transition boundary by adjusting

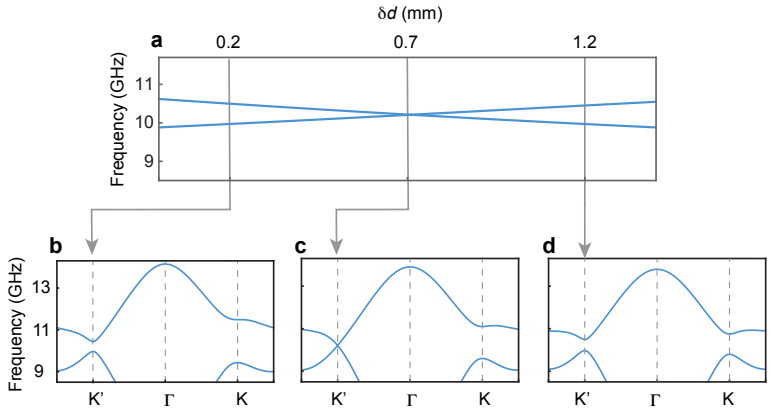

FIG. S1. **Realization of type-A PVHSM by tuning $\mathcal{P}$-breaking strength.** **a**, Eigenfrequencies at the K′ point as functions of radius difference ($\delta d = d_2 - d_1$), illustrating the band inversion process controlled by $\mathcal{P}$-breaking strength. **b-d**, Band structures of the PC with radius differences δd = 0.2mm, 0.7mm, and 1.2mm, respectively. Throughout this tuning process, external magnetic fields remain fixed at $H_{\text{ext}} = 1100\,\text{Oe}$, while cylinder radii are $d_1 = d_0 - \delta d/2$ and $d_2 = d_0 + \delta d/2$, where $d_0 = 3.35\,\text{mm}$.

the radius difference between two YIG cylinders, $\delta d = d_2 - d_1$. Taking type-A PVHSM as an example, the continuous parameter range is shown by the black line segment in Fig. S2a, with endpoints corresponding to $\delta d = 0.3$ (A_I in phase-I) and $\delta d = 1.1$ (A_IV in phase-IV). Figures S2b and c display the corresponding bulk band structures for A_I and A_IV. Figure S2d shows how the upper and lower band edges at K and K′ points evolve with δd in type-A PC, with $\delta d = 0.7$ marking the critical point where $\mathcal{P}$- and $\mathcal{T}$-breaking effects are balanced.

Applying $\mathcal{P}$ or $\mathcal{T}$ operations to A_I and A_IV generates three additional structures that deviate from PVHSMs (represented by the black dots and circles near phase boundaries in Fig. S2a). Figure S2e(f) shows the band structure when arranging these four black dots (circles) as topological photonic highways, revealing that the deviation from exact PVHSMs barely affects the band structures. However, as exemplified by Figs. S2h and i, since all domains become insulators when parameters deviate from PVHSMs, the physical essence of the waveguide states undergoes an abrupt transition from uniform extended states to interface states, characterized by field maxima at interfaces and exponential decay on both sides. For instance, in Fig. S2h, the original extended waveguide modes in A and D domains become interface states between A and D, while extended modes in C and B become interface states between C and B. In Fig. S2i, extended modes in A and B transform to A-B interface states, while those in C and D become C-D interface states. Nevertheless, Fig. S2g reveals that the centroids of the waveguide modes shift smoothly from each domains center toward its boundary as δd varies. Consequently, for small deviations from PVHSMs, although the waveguide modes exhibit their field maxima at the interfaces, the field distributions remain predominantly confined within each single domain, maintaining the effective functionality

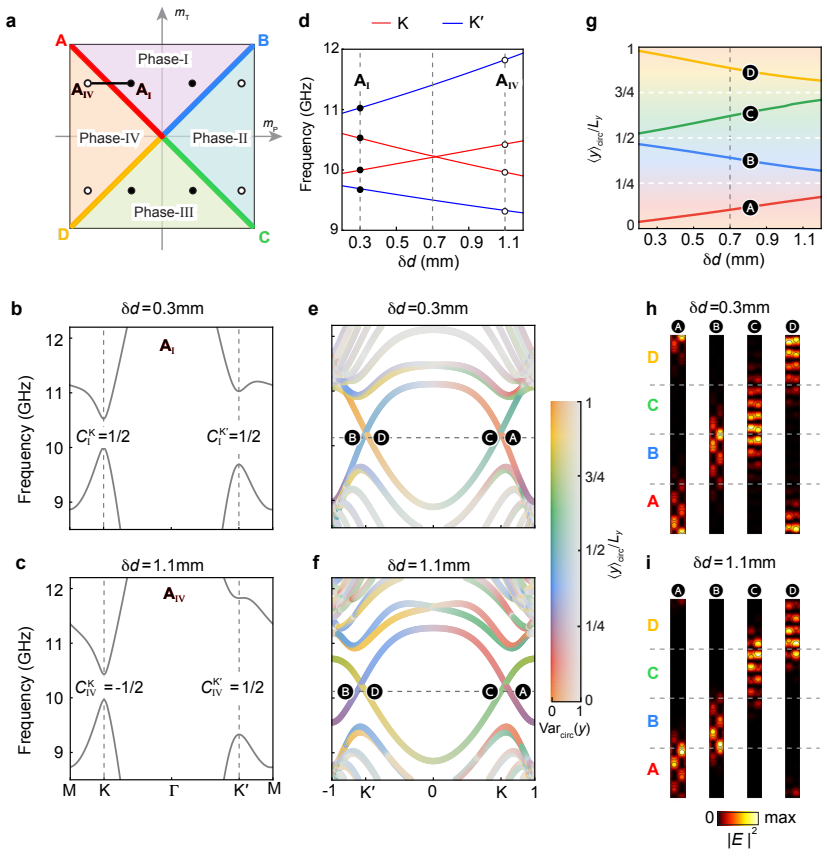

FIG. S2. **Evolution of topological photonic highways deviating from exact $\mathcal{P}$- and $\mathcal{T}$-breaking balance.** **a**, Phase diagram in the parameter space (m_P, m_T). **b**,**c**, Band structures for A_I-type PC ($\delta d = 0.3\,\mathrm{mm}$) and A_{IV}-type PC ($\delta d = 1.1\,\mathrm{mm}$). **d**, Band edge evolution at K and K′ points as a function of δd near the phase transition boundary A (corresponding to the line segment in **a**). **e**,**f**, Band structure of the superlattices formed by four PC types marked by the four black dots (for **e**) and by the four circles (for **f**) in **a**. **g**, The intensity centroids of the four waveguide modes at $f = 10.14\,\mathrm{GHz}$ versus δd. **h**,**i**, Eigenfields of the four waveguide modes indicated in **e** and **f**.

of topological photonic highways.

S2. Quantitative characterization of inter-domain crosstalk within topological photonic highways

We define S-parameters by treating a selected region of the topological photonic highway as the scattering object (see, e.g., the region of disorders in Fig. S3a), with each unidirectional eigen waveguide mode at both ends of the region serving as independent input and output channels. This methodology directly characterizes the intrinsic crosstalk and quantifies inter-domain and inter-valley scattering induced by internal disorder, defects, or shape variations. This approach, however, has an inherent limitation: since it assumes unidirectional propagation in each waveguide domain as a known condition, it cannot serve to validate the structures domain-selective unidirectional

transmission characteristics. Nevertheless, this method is very useful when our primary focus is on the intrinsic inter-domain and inter-valley crosstalks within the topological photonic highway.

A. S-parameters characterizing intrinsic crosstalk inside topological photonic highways

We present the S-parameter calculation methodology for topological multi-lane highways, using the configuration shown in Fig. S3a as our model system. We focus on the frequency window (9.8–10.6 GHz) supporting domain-selective one-way single modes. To quantify inter-channel scattering and crosstalk at a frequency f, we employ the four eigenmodes of the unperturbed structure $|\mathrm{A_4B_4C_4D_4}|_1$ as independent input and output channels: $\left|E_z^i(k_x)\right\rangle$ ($i \in \{\mathrm{A},\mathrm{B},\mathrm{C},\mathrm{D}\}$). These eigenmodes are predominantly localized within individual waveguides, establishing a direct correspondence between the four channels and the four waveguides. Notably, due to the unidirectional nature of these waveguides, each port supports exclusively either an input or an output mode (Fig. S3a). Therefore, the total field at the left and right sides of the disordered region can be expressed as

$$\left|E_z^L\right\rangle = c_L^{\mathrm{A}}\left|E_z^{\mathrm{A}}\right\rangle + c_L^{\mathrm{B}}\left|E_z^{\mathrm{B}}\right\rangle + c_L^{\mathrm{C}}\left|E_z^{\mathrm{C}}\right\rangle + c_L^{\mathrm{D}}\left|E_z^{\mathrm{D}}\right\rangle, \tag{S1}$$

$$\left|E_z^R\right\rangle = c_R^{\mathrm{A}}\left|E_z^{\mathrm{A}}\right\rangle + c_R^{\mathrm{B}}\left|E_z^{\mathrm{B}}\right\rangle + c_R^{\mathrm{C}}\left|E_z^{\mathrm{C}}\right\rangle + c_R^{\mathrm{D}}\left|E_z^{\mathrm{D}}\right\rangle. \tag{S2}$$

Note that near the Dirac frequency, the intersection of waveguide bands at each valley creates a mini-gap. In this vicinity of mini-gap, the true eigenstates exist as linear superpostions of waveguide modes (modes A and C at K point, modes B and D at K′ point). Therefore, to obtain independent waveguide modes localized in individual waveguides, linear combinations of the directly calculated eigenstates must be performed near the mini-gap.

The crosstalk and inter-domain scattering among the four waveguides can be characterized by the scattering matrix between the four eigen-waveguide modes,

$$\boldsymbol{c}_{\mathrm{out}} = \boldsymbol{S}\,\boldsymbol{c}_{\mathrm{in}}, \tag{S3}$$

where $\boldsymbol{c}_{\mathrm{out}} = \left(c_L^{\mathrm{A}}, c_R^{\mathrm{B}}, c_R^{\mathrm{C}}, c_L^{\mathrm{D}}\right)^{\top}$ and $\boldsymbol{c}_{\mathrm{in}} = \left(c_R^{\mathrm{A}}, c_L^{\mathrm{B}}, c_L^{\mathrm{C}}, c_R^{\mathrm{D}}\right)^{\top}$ denote the coefficient vectors at the input and output ports, respectively. Here, $\boldsymbol{S} = (S_{ij})$ denotes the scattering matrix, with its element S_{ij} ($i, j \in \{\mathrm{A},\mathrm{B},\mathrm{C},\mathrm{D}\}$) representing the S-parameter from the input channel j to the output channel i.

In numerical simulations, the superposition coefficients of waveguide modes, $c_{L|R}^i(f)$, at the left or right side can be obtained by projecting the total field $E_z^{L|R}(f,\mathbf{r})$ onto each eigenstate:

$$c_{L|R}^i(f) = \int_{Q_{L|R}} \mathrm{d}^2\mathbf{r}\; E_z^i\big(k_x(f),\mathbf{r}\big)^*\,\varepsilon(\mathbf{r})\,E_z^{L|R}(f,\mathbf{r}), \qquad i \in \{\mathrm{A},\mathrm{B},\mathrm{C},\mathrm{D}\}. \tag{S4}$$

Here, the eigen electric fields satisfy the orthonormality

$$\int_{\mathbb{R}^2} \mathrm{d}^2\mathbf{r}\; E_z^i(k_x,\mathbf{r})^*\,\varepsilon(\mathbf{r})\,E_z^j(k_x',\mathbf{r}) = \delta_{ij}\,\delta(k_x-k_x'). \tag{S5}$$

For the projection calculations, we select two finite rectangular regions $Q_{L|R}$ (indicated by the gray

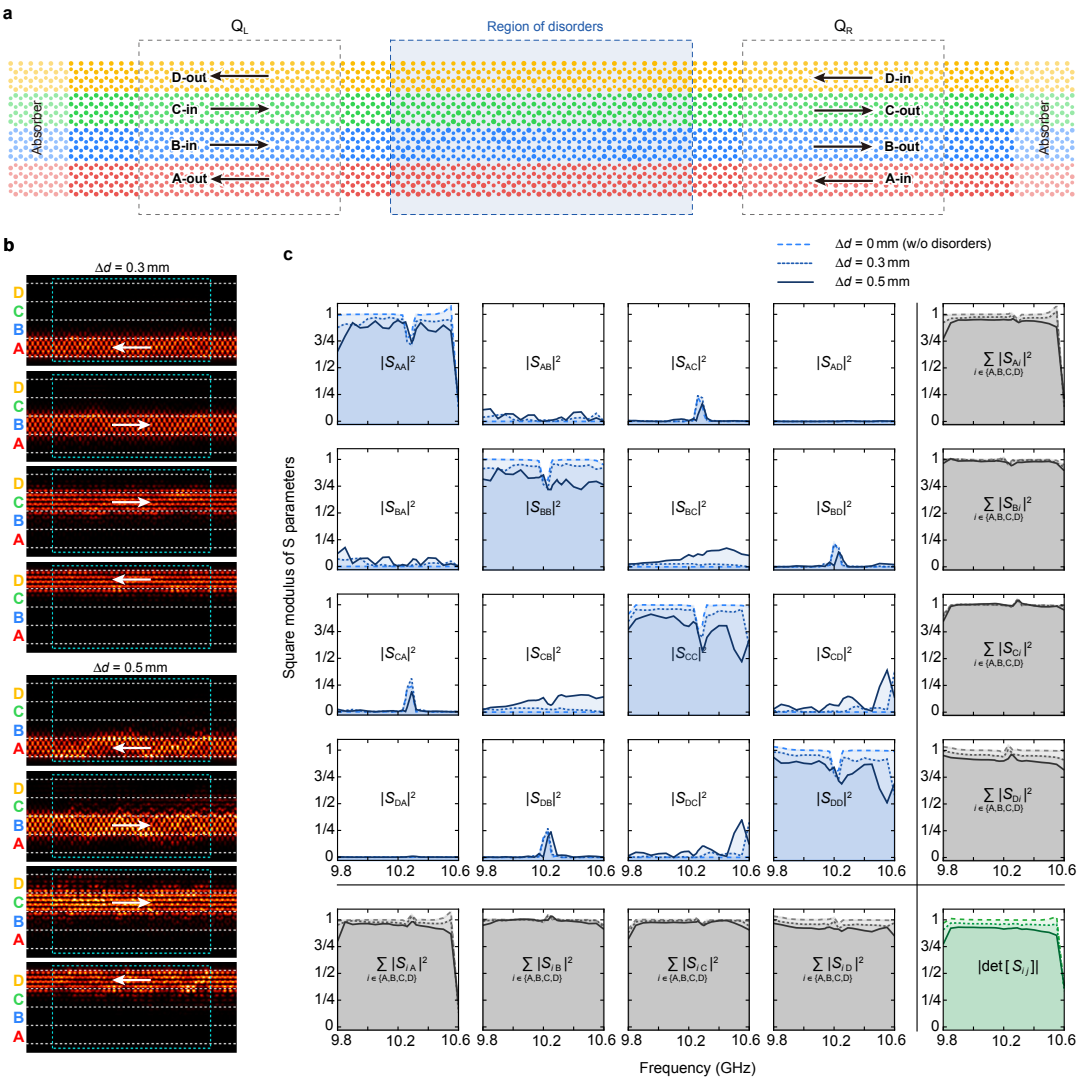

FIG. S3. **S-parameters for disordered waveguides.** **a**, Schematic of a topological photonic multi-lane highway $|\mathrm{A_4B_4C_4D_4}|_1$ with random rod radius variations. Rod radii are uniformly distributed within $d_1 \in [3\,\mathrm{mm} \pm \Delta d/2]$ and $d_2 \in [3.7\,\mathrm{mm} \pm \Delta d/2]$ in the region enclosed by blue dashed lines. The gray dashed rectangles ($Q_{L|R}$) with size $20a \times 10\sqrt{3}a$ denote the input and output regions for calculating the projection onto eigenstates. **b**, Simulated field distributions excited in different domains at $f = 10.35\,\mathrm{GHz}$ for the disorder strengths $\Delta d = 0.3\,\mathrm{mm}$ (upper panel) and $\Delta d = 0.5\,\mathrm{mm}$ (lower panel), respectively. **c**, Calculated scattering parameters for disorder strengths $\Delta d = 0, 0.3, 0.5\,\mathrm{mm}$ as functions of frequency. The blue curves denote the square moduli of the scattering-matrix elements. The gray curves denote the sum of squares of each row and column. The green curves denote the norm of the scattering matrix determinant.

dashed boxes in Fig. S3a) at the left and right sides as integration domains. The rectangular regions $\Omega_{L|R}$ must extend sufficiently in the x direction to ensure the validity of the orthonormality relation in Eq. (S5). Through four separate excitations with the source placed in different waveguides, we obtain four sets of linearly independent input and output coefficient vectors $\boldsymbol{c}_{\text{in}}^{m}$ and $\boldsymbol{c}_{\text{out}}^{m}$ ($m \in \{1,2,3,4\}$), which form two invertible square matrices

$$\boldsymbol{C}_{\text{in}} = \left(\boldsymbol{c}_{\text{in}}^{1}, \boldsymbol{c}_{\text{in}}^{2}, \boldsymbol{c}_{\text{in}}^{3}, \boldsymbol{c}_{\text{in}}^{4}\right), \qquad \boldsymbol{C}_{\text{out}} = \left(\boldsymbol{c}_{\text{out}}^{1}, \boldsymbol{c}_{\text{out}}^{2}, \boldsymbol{c}_{\text{out}}^{3}, \boldsymbol{c}_{\text{out}}^{4}\right),$$

and satisfy

$$\boldsymbol{C}_{\text{out}} = \boldsymbol{S} \cdot \boldsymbol{C}_{\text{in}}. \tag{S6}$$

Then, the scattering matrix can be extracted as

$$\boldsymbol{S} = \boldsymbol{C}_{\text{out}} \cdot \boldsymbol{C}_{\text{in}}^{-1}. \tag{S7}$$

B. S-parameters for straight topological photonic highways with or without disorders

To evaluate the intrinsic and disorder-induced inter-channel scatterings in straight topological photonic highways, we have studied the structure $|\text{A}_4\text{B}_4\text{C}_4\text{D}_4|$ with or without disorders, as shown in Fig. S3a. The disorders were introduced as random diameter fluctuations of both YIG rod types within the dashed blue box. The diameters of two types of YIG rods are homogeneously distributed in the intervals $d_1 \in [3\,\text{mm} \pm \Delta d/2]$ and $d_2 \in [3.7\text{mm} \pm \Delta d/2]$, respectively.

Figure S3c illustrates the frequency dependence of the scattering matrix for the straight waveguide region with different disorder strengths Δd = 0, 0.3, and 0.5. The near-zero S-parameters $|S_{i,(i+1)\text{mod}4}|$ at $\Delta d = 0$ demonstrate that inter-valley scattering is negligible in the absence of disorder. However, the inter-valley scattering intensity increases systematically with disorder magnitude. For example, in the third column, $|S_{\text{BC}}|^2$ and $|S_{\text{DC}}|^2$ show significant enhancement with increasing Δd. This behavior indicates disorder-mediated scattering from K-valley modes in domain C to K′-valley modes in domains B and D.

Another noteworthy spectral signature occurs near the Dirac frequency (10.2 GHz), characterized by the dips in diagonal S-parameters coinciding with peaks in non-diagonal parameters $S_{i,(i+2)\ \text{mod}\ 4}$. This behavior presents even in disorder-free waveguides ($\Delta d = 0$), indicating significant intrinsic inter-domain crosstalk at the intersection of counter-propagating waveguide bands within the same valley (between A and C, or B and D waveguides). Although its existence independent of disorder and remains relatively stable with increasing disorder strength, the crosstalk presents in a narrow frequency range near the Dirac frequency (< 0.1 GHz) presents a clear advantage over the broadband crosstalk characteristic of conventional parallel waveguides. Furthermore,

in Section S3 A 2, we will quantitatively demonstrate that this intrinsic intra-valley crosstalk in the topological photonic highway is significantly weaker than that in topological interface-state waveguide arrays constructed using photonic topological insulators with identical $\mathcal{T}$- or $\mathcal{P}$-breaking strengths and identical domain widths as in PVHSMs.

C. S-parameters for topological photonic highways with 120° sharp bend structure and a geometrically engineered structure

Figures S4 and S5 present scattering matrix calculations for the 120° sharp bend structure (Fig. 4 of main text) and the field morphing structure (Fig. 5 of main text), respectively. The results demonstrate that sharp bends and geometric variations induce negligible inter-valley scattering ($|S_{i,(i+1) \bmod 4}|^2 < 2\%$) across most frequencies. However, notable intra-valley crosstalk caused by the band crossing of counter-propagating waveguide modes still appears near the Dirac frequency (10.2 GHz) as in the straight waveguide scenario, evidenced by dips in $S_{i,i}$ and peaks in $S_{i,(i+2) \bmod 4}$.

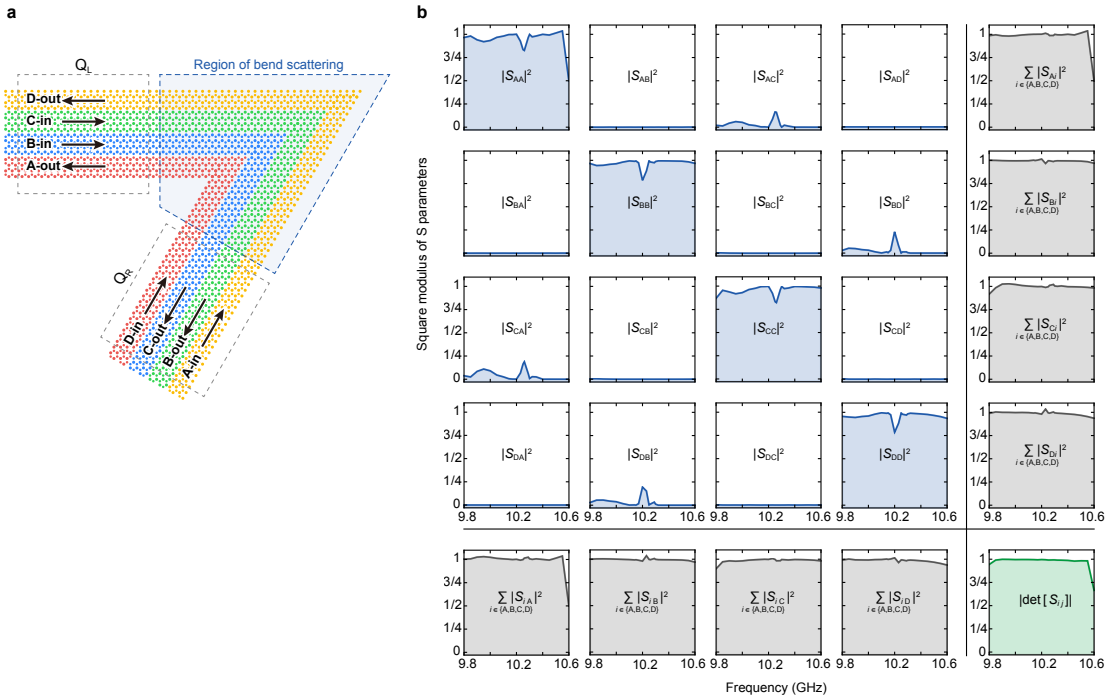

FIG. S4. **S-parameters for a 120° bend. a**, Schematic of a topological photonic multi-lane highway $|A_4B_4C_4D_4|_1$ with a 120° sharp bend. The blue dashed polygon indicates the region of bend scattering. The gray dashed rectangles ($Q_{L|R}$) denote the input and output regions for eigenstate projection calculations. **b**, Scattering parameters of the bending structure in **a** as functions of frequency within 9.8 – 10.6 GHz. The blue curves represent the square moduli of the scattering-matrix elements. The gray curves denote the sum of squares for each row and column of the scattering matrix. The green curve denotes the norm of the scattering matrix determinant.

However, this crosstalk remains confined to a narrow frequency range around the Dirac frequency, resulting in significantly less impact compared to conventional parallel waveguides.

The scattering process largely preserves energy conservation, as shown by the gray curves and

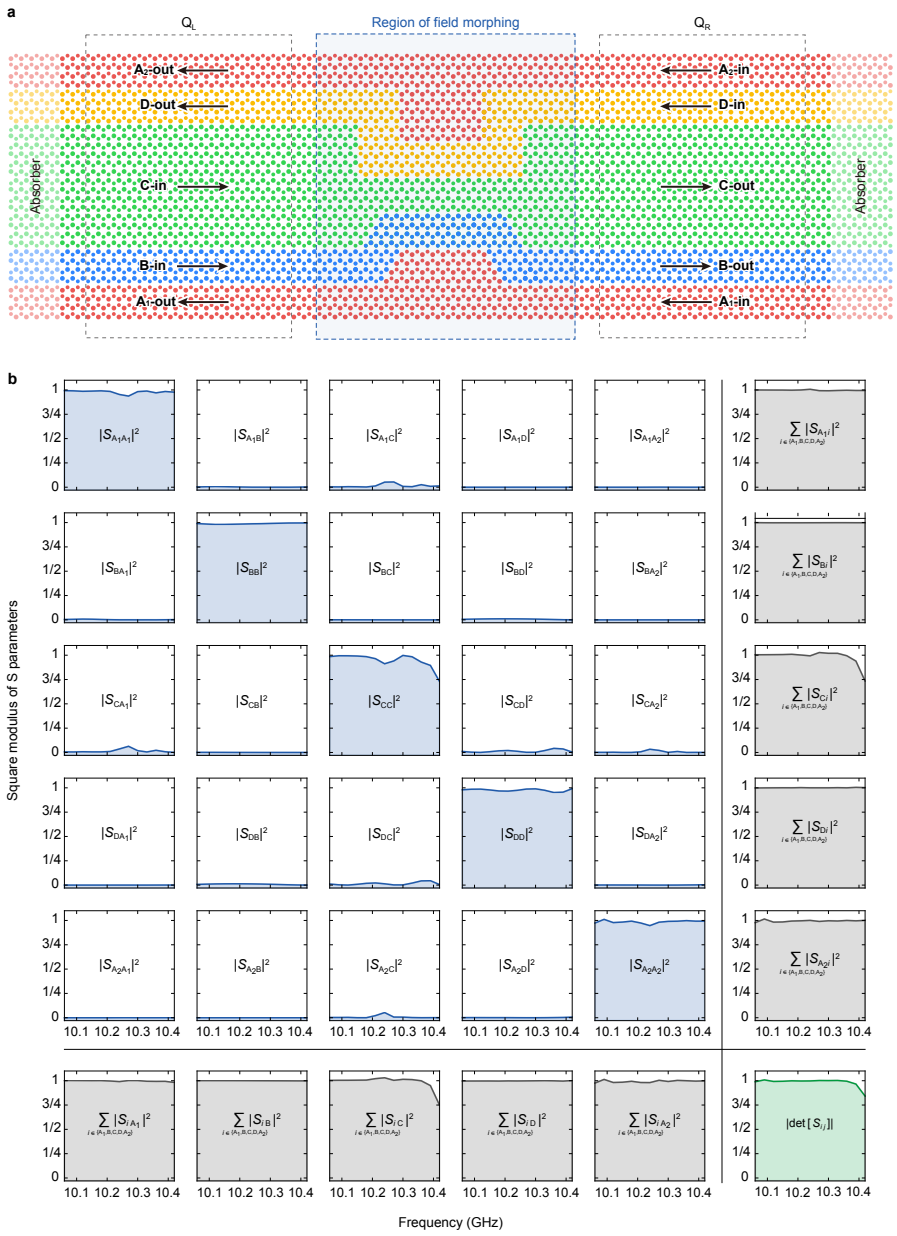

FIG. S5. **S-parameters for a geometrically engineered topological photonic multi-lane highway.** **a**, Schematic of a geometrically engineered topological photonic highway with the same shape as in Fig. 5 of the main text. The blue dashed rectangle indicates the region of field morphing. The gray dashed rectangles ($Q_{L|R}$) denote the input and output regions for eigenstate projection calculations. **b**, Scattering parameters of the structure in a as functions of frequency with 10.1 – 10.4 GHz. The blue curves represent the square moduli of the scattering-matrix elements. The gray curves denote the sum of squares for each row and column of the scattering matrix. The green curve denotes the norm of the scattering matrix determinant.

the green determinant curves in Figs. S4 and S5, with deviations primarily attributable to air radiation losses at bends or deformations. The notable violations of energy conservation in $|\det[\boldsymbol{S}]|$ curves at 10.6 GHz in Fig. S4b and 10.4 GHz in Fig. S5b arise from higher-order waveguide modes excited near the band edge, which were not included as energy channels in the scattering matrix calculations.

D. Coupled-mode analysis for intra-valley crosstalk

The preceding calculations demonstrate that the inter-valley scattering between adjacent domains is considerably weak in most cases. However, near the Dirac frequency, two counter-propagating waveguide modes within the same valley exhibit significant intra-valley crosstalk. This arises because these two kink states, localized at a pair of next-nearest-neighbor domains, couple through evanescent waves across the intermediate domain and open a mini-gap at the band-crossing point near the Dirac frequency. In what follows, we rigorously analyze this mode-coupling-induced crosstalk using coupled-mode theory and compare the results with numerical simulations.

Analytic solution of ideal domain-wall state. We start by considering the 2D Dirac Hamiltonian (e.g. K′ valley) for a single domain wall homogeneously extended along the x-direction:

$$\mathcal{H}^{K'}(y) = v_D\left(-\delta k_x \hat{\sigma}_x - i\,\partial_y \hat{\sigma}_y\right) + m(y)\hat{\sigma}_z. \tag{S8}$$

For example, the mass distribution for an ideal single kink state (say state localied in domain B) is described by the piecewise function:

$$m_B(y) = \begin{cases} -m_0, & \Delta y_B > W/2 \qquad \text{(domain C)} \\ 0, & -W/2 \le \Delta y_B \le W/2 \qquad \text{(domain B)} \\ m_0, & \Delta y_B < -W/2 \qquad \text{(domain A)} \end{cases} \tag{S9}$$

where $\Delta y_B = y - y_B$ with y_B denoting the center of domain B, and domains A and C are ideally set as semiinfinite. The analytic solution of the dispersion and profile of the domain state are given by

$$\delta\omega_B = v_D\,\delta k_x, \qquad \Psi_B(x,y) = A\psi(\Delta y_B)\begin{pmatrix} 1 \\ -1 \end{pmatrix} e^{i\delta k_x x}, \tag{S10}$$

where the normalization coefficient $A = 1/\sqrt{2\,(W + v_D/m_0)}$, and the spatial profile

$$\psi(\Delta y) = \begin{cases} \exp\Big[-\dfrac{m_0}{v_D}\,(\Delta y - W/2)\Big], & \Delta y > W/2 \\ 1, & -W/2 \le \Delta y \le W/2 \\ \exp\Big[\dfrac{m_0}{v_D}\,(\Delta y + W/2)\Big], & \Delta y < -W/2 \end{cases} \tag{S11}$$

Similarly, the ideal kink state at domain D is described by

$$\delta\omega_D = -v_D\,\delta k_x, \qquad \Psi_D(x,y) = A\psi(\Delta y_D)\begin{pmatrix}1\\1\end{pmatrix}e^{i\delta k_x x}, \tag{S12}$$

with $\Delta y_D = y - y_D$ and y_D denoting the center of domain D.

Effective Hamiltonian of two counter-propagating domain-walls states. Next, we consider the coupling between the kink states localized at two next-nearest neighboring domains characterized by the mass distribution (see Fig. S6a)

$$m(y) = \begin{cases} -m_0, & y > (W + d/2) & \\ 0, & d/2 \le y \le (W + d/2) & (2^{\text{nd}}\text{ kink}) \\ m_0, & -d/2 < y < d/2 & (\text{Barrier}) \\ 0, & -(W + d/2) \le y \le -d/2 & (1^{\text{st}}\text{ kink}) \\ -m_0, & y < -(W + d/2) & \end{cases} \tag{S13}$$

Referring to the topological photonic highways system, the five piecewise intervals (from bottom to top) correspond to domains A, B (1^{st} kink), C (barrier), D (2^{nd} kink), and A, respectively, and the coupling distance $d = W$. This profile creates two topological kinks with opposite valley Chern number differences. Under ideal single kink approximation, the first kink (domain B) supports a right-propagating mode $\Psi_B(y)$ with velocity v_D and spinor $|-\rangle = \frac{1}{\sqrt{2}}(1,-1)^T$ (blue curve in Fig. S6a illustrates). The second kink (domain D) supports a left-propagating mode $\Psi_D(y)$ with velocity $-v_D$ and orthogonal spinor $|+\rangle = \frac{1}{\sqrt{2}}(1,1)^T$ (yellow curve in Fig. S6a). Note that due to the opposite spinors of the two ideal states, their direct overlap integral exactly vanishes: $\langle\Psi_B|\Psi_D\rangle \equiv 0$.

Supposing that the coupled wavefunction can be approximately expressed as the superposition of two uncoupled ideal kink states $\Psi = a_1\Psi_B + a_2\Psi_D$, we can construct the effective coupled Hamiltonian via the coupled-mode theory:

$$H_{\text{eff}}(\delta k_x) = \left(\langle\Psi_i|H^{K'}(y)|\Psi_j\rangle\right) = \begin{pmatrix} v_D\delta k_x & t \\ t & -v_D\delta k_x \end{pmatrix}. \tag{S14}$$

The coupling coefficient t is calculated via the overlap integral

$$\begin{aligned} t &= \langle\Psi_B|H^{K'}(y)|\Psi_D\rangle = \langle\Psi_B|H_B^{K'}(y) + \delta m(y)\hat{\sigma}_z|\Psi_D\rangle \\ &= -v_D k_x\langle\Psi_B|\Psi_D\rangle + \langle\Psi_B|\delta m(y)\hat{\sigma}_z|\Psi_D\rangle \\ &= A^2\langle\psi(\Delta y_B)|\delta m(y)|\psi(\Delta y_D)\rangle\langle-|\hat{\sigma}_z|+\rangle \\ &= 2A^2\langle\psi(\Delta y_B)|\delta m(y)|\psi(\Delta y_D)\rangle. \end{aligned} \tag{S15}$$

where $\delta m(y) = m(y) - m_B(y) = \begin{cases} 0, & y < d/2 \\ -m_0, & d/2 \le y \le (W + d/2) \\ -2m_0, & y > (W + d/2) \end{cases}$. Therefore, we obtain

$$\begin{aligned} t &= 2A^2 \langle \psi(\Delta y_B) | \delta m(y) | \psi(\Delta y_D) \rangle \\ &= 2A^2 \int_{d/2}^{+\infty} \psi(y + (W/2 + d))\, \delta m(y) \psi(y - (W/2 + d))\, dy \\ &= -2A^2 v_D e^{-\frac{m_0 d}{v_D}} = -\frac{v_D}{W + v_D/m_0} e^{-\frac{m_0 d}{v_D}}. \end{aligned} \tag{S16}$$

As expected, the coupling strength $|t|$ decays exponentially with the barrier width d. Diagonalizing H_{eff} yields the coupled energy bands

$$\delta\omega_{\pm}(\delta k_x) = \pm\sqrt{(v_D \delta k_x)^2 + |t|^2}, \tag{S17}$$

which open a mini bandgap of $\Delta\omega = 2|t|$ at $\delta k_x = 0$ (as illustrated in Fig. S6b).

Crosstalk of two counter-propagating kink states. We now consider the crosstalk between the two waveguide modes at a given frequency $\omega = \omega_D + \delta\omega$ (ω_D is the Dirac frequency)

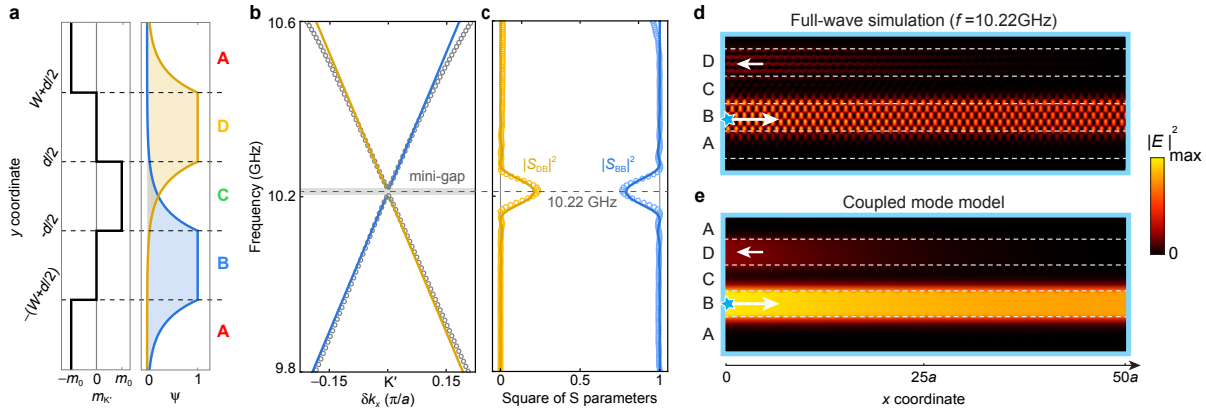

FIG. S6. **Coupled mode estimation of intra-valley crosstalk. a**, Effective mass distribution of two mass kinks that support two coupled kink states localized at domains B and D, respectively. Blue and yellow curves: mode profiles of two individual uncoupled kink states as solutions of ideal single kinks at B and D. **b**, Band structure of the topological photonic highway $|A_4B_4C_4D_4|$ (gray circles) and the corresponding coupled mode effective Hamiltonian (solid curves). The blue-to-yellow blending color indicates the intensity fraction distributed on the two kink basis states. **c**, Simulated (circles) and coupled-mode-estimated (solid lines) square of S parameters $|S_{DB}|^2$, $|S_{BB}|^2$ of a straight photonic highway with length $L_w = 50a$. **d**,**e**, Full-wave (**d**) and coupled-mode results (**e**) of the field distributions at 10.22 GHz in the topological photonic highway with field input at the left end of domain B. The coupled mode parameters are extracted from the bulk-band structure: $m_0 = 1.8\pi$ GHz, $v_D = 16.2\pi \times 10^6$ Hz $\cdot$ m, $W = d = 2\sqrt{3}a$.

during propagation. Because the two modes are counter-propagating, this system acts as a contra-directional coupler. Let $a_2(x)$ be the rightward mode (injected signal) and $a_1(x)$ be the leftward mode (crosstalk). According to the effective Hamiltonian by replacing $\delta k_x \to -i\partial_x$:

$$H_{\text{eff}}(-i\partial_x)\begin{pmatrix} a_1 \\ a_2 \end{pmatrix} = (-iv_D\partial_x\hat{\sigma}_z + t\hat{\sigma}_x)\begin{pmatrix} a_1 \\ a_2 \end{pmatrix} = \delta\omega\begin{pmatrix} a_1 \\ a_2 \end{pmatrix}. \tag{S18}$$

The spatial coupled mode equation at a frequency can be derived as

$$\partial_x\begin{pmatrix} a_1 \\ a_2 \end{pmatrix} = \left(i\frac{\delta\omega}{v_D}\hat{\sigma}_z + \frac{t}{v_D}\hat{\sigma}_y\right)\begin{pmatrix} a_1 \\ a_2 \end{pmatrix} = \begin{pmatrix} i\delta\omega/v_D & -it/v_D \\ it/v_D & -i\delta\omega/v_D \end{pmatrix}\begin{pmatrix} a_1 \\ a_2 \end{pmatrix}. \tag{S19}$$

For a waveguide of length L_w, we apply the two-point boundary conditions: $a_1(0) = 1$ (single-port injection) and $a_2(L_w) = 0$ (no backward injection from the output end). Then, the analytic solution of this boundary condition problem is obtained

$$a_1(x) = \frac{\frac{\Delta k}{2}\cos(\Delta k(L_w - x)/2) - \frac{i\delta\omega}{v_D}\sin(\Delta k(L_w - x)/2)}{\frac{\Delta k}{2}\cos(\Delta k L_w/2) - \frac{i\delta\omega}{v_D}\sin(\Delta k L_w/2)}, \tag{S20}$$

$$a_2(x) = \frac{-i\frac{t}{v_D}\sin(\Delta k(L_w - x)/2)}{\frac{\Delta k}{2}\cos(\Delta k L_w/2) - \frac{i\delta\omega}{v_D}\sin(\Delta k L_w/2)}. \tag{S21}$$

where $\Delta k = \frac{2}{v_D}\sqrt{\delta\omega^2 - t^2} = 2\delta k_x$ represents the momentum difference of two counter-propagating modes at the frequency $\omega = \omega_D + \delta\omega$. Within the minigap $\delta\omega^2 - t^2 < 0$, we take $\Delta k = i\frac{2}{v_D}\sqrt{t^2 - \delta\omega^2}$.

The **intra-valley crosstalk** of the two counter-propagating modes is characterized by the S-parameter S_{DB}, whose square equals the fraction of energy reflected into the backward-propagating mode at the input port, i.e., $|S_{DB}|^2 = |a_2(0)|^2/|a_1(0)|^2$. The evolution behavior strictly depends on the injection frequency:

$$|S_{DB}|^2 = \frac{t^2\sin^2(\Delta k L_w/2)}{(\delta\omega^2 - t^2) + t^2\sin^2(\Delta k L_w/2)}. \tag{S22}$$

The total energy flux conservation through each transverse section requires that $|a_1(x)|^2 - |a_2(x)|^2 = J = \text{const.}$, which leads to $|a_2(0)|^2 = |a_1(0)|^2 - J = 1 - |a_1(L_w)|^2$. Consequently, the transmittance $|S_{BB}|^2 = |a_1(L_w)|^2/|a_1(0)|^2 = 1 - |S_{DB}|^2$ when ignoring other mode coupling and leakage mechanisms.

Equation (S22) reveals that when the frequency lies outside the mini-bandgap, the reflectance $|S_{DB}|^2$ fluctuates with the waveguide length. However, $0 \le |S_{DB}|^2 \le \frac{t^2}{\delta\omega^2} < 1$ indicates that the energy can never completely transfer to the backward channel and the upper bound of backward

crosstalk outside the minigap is independent of the waveguide length, which is sharply different from the co-directional coupling case, where energy transfers 100% periodically between the two waveguides. In particular, when the injection frequency far always from the gap ($t^2 \ll \delta\omega^2$), the crosstalk becomes negligibly small. In contrast, when the frequency lies inside the mini-bandgap, the injected wave becomes an evanescent mode and decays exponentially along x. Therefore, the **analytic result confirms that only a small fraction of the frequency range close to the mini-bandgap exhibits remarkable crosstalk.**

By substituting the exact parameters extracted from the bulk band structure into Eq. (S22), we obtain $|S_{DB}|^2$ and $|S_{BB}|^2$ under the coupled-mode approximation (Fig. S6c), which show excellent agreement with the numerically simulated curves. This confirms that the crosstalk strength can be fully explained by the coupling between two isolated kink states. Meanwhile, Figs. S6d,e demonstrate that the propagating field distributions from full-wave simulations and the coupled-mode model also agree well.

S3. Comparison between topological photonic highways and other systems or mechanisms.

A. Comparison between topological photonic highways and conventional topological interface-state waveguides

1. Advantages and disadvantages of topological photonic highways compared to conventional topological interface-state waveguides

In this section, we summarize the advantages and disadvantages of topological photonic multi-lane highways compared to conventional topological edge-state waveguides.

Advantages:

1. **Enhanced spatial efficiency and integration capability.** By utilizing photonic valley half-semimetals (PVHSMs), which possess the unique spectral characteristic of simultaneously functioning as an insulator cladding for neighboring waveguides while itself serves as a unidirectional waveguide, the topological photonic highways achieve robust unidirectional transport with 100% spatial utilization. In contrast, conventional chiral topological edge states are confined to interfaces between sufficiently thick topological insulators, limiting their spatial efficiency.

2. **Novel field morphing functionality enabled by geometric flexibility.** A distinctive advantage of topological photonic highways lies in their unique domain adaptability: each PVHSM domain can undergo arbitrary reshaping and resizing while preserving unidirectional transport characteristicsa feature unavailable in conventional topological edge states. This

additional geometric degree of freedom, coupled with independent configuration of multiple parallel domains, enables sophisticated functionalities including field morphing, focusing, and defocusing, facilitating ultra-compact, domain-specific wave field engineering.

3. **More uniform field distributions and larger mode volumes result in enhanced power-handling capability.** The uniform field distributions in topological photonic highways yield larger mode volumes compared to conventional topological edge states. This characteristic enables higher energy flux thresholds while maintaining the materials local damage threshold (local field intensity threshold), providing advantages in high-power applications. Moreover, the increased mode volume reduces nonlinear distortion during high-power transmission, leading to improved long-distance transmission performance.

4. **The synergistic effect of $\mathcal{T}$ and $\mathcal{P}$ breaking doubles the valley gap width, significantly enhancing the maximum spatial channel density.** The formation mechanism of PVHSMs provides an intrinsic advantage: the gapped valley bandgap width in PVHSMs equals the sum of the independent $\mathcal{T}$-breaking and $\mathcal{P}$-breaking bandgaps. This results in valley bandgaps twice as wide as those achieved by breaking either time-reversal or spatial inversion symmetry alone with equivalent strength. This directly shortens the mode localization length, leading to superior field insulation (see details in Section S3 A 2). Given that $\mathcal{T}$-breaking is typically constrained by the limited strength of magneto-optical responses, PVHSMs offer a fundamental pathway to larger insulating bandgaps without requiring enhanced magneto-optical materials, enabling effective crosstalk suppression with thinner domain widths than those required in conventional interface-state waveguide arrays.

Disadvantages:

Constrained one-way single-mode bandwidth. Unlike conventional topological edge states where the unidirectional window spans the entire bulk bandgap, the topological photonic highway exhibits an inverse relationship between the domain width and the single-mode bandwidth. As the waveguide domain is widened, the frequency window for strictly single-mode, unidirectional propagation narrows (see Extended Data Fig. 1). However, it is crucial to note that while the unidirectional single-mode bandwidth decreases with increasing domains width, the total frequency range supporting cladding-free waveguiding (either unidirectional or bidirectional) remains constant and equal to the bulk gapwidth of the insulating valley in PVHSMs, regardless of the domain thickness. As demonstrated in Extended Data Fig. 2, when the single-mode unidirectional window is exceeded (Extended Data Fig. 2a), the waveguide transitions to supporting multi-mode and bidirectional propagation, but it continues to guide light effectively without claddings (Extended Data Fig. 2b-e).

2. Quantitative evidence of topological photonic highways on enhancing maximum spatial channel density

The formation mechanism of PVHSMs endows topological photonic highways with distinct advantages for maximizing spatial channel density while maintaining equivalent inter-domain crosstalk performance compared to conventional topological interface waveguides. Specifically, the synergistic effect of $\mathcal{T}$ and $\mathcal{P}$ breakings doubles the valley gap width, providing the maximum attainable valley gap in photonic graphenes for given symmetry-breaking strengths, as illustrated in Fig. S7. The resulting twofold increase in the maximal imaginary component of complex wave vectors (Fig. S7d) significantly reduces mode localization length within the valley gap compared to single-symmetry breaking insulators, thereby suppressing inter-domain crosstalks caused by intra-valley couplings.

To quantitatively validate the above analysis, we design a conventional multilane topological interface-state waveguide as a benchmark for comparison. As shown in Fig. S8, this structure comprises photonic insulators that break either $\mathcal{P}$ or $\mathcal{T}$ symmetry–but not both simultaneously–arranged in the sequence I, II, III, IV, I (the Roman numerals correspond to the four gapped phases in Fig. S8a). This configuration generates four distinct topological interface modes (labeled as ❶, ❷, ❸, ❹ in Figs. S8c and d) at the boundaries between adjacent domains. For clarity, we omit the lighter gray bands in Fig. S8d, which represent edge states localized at the outermost boundaries

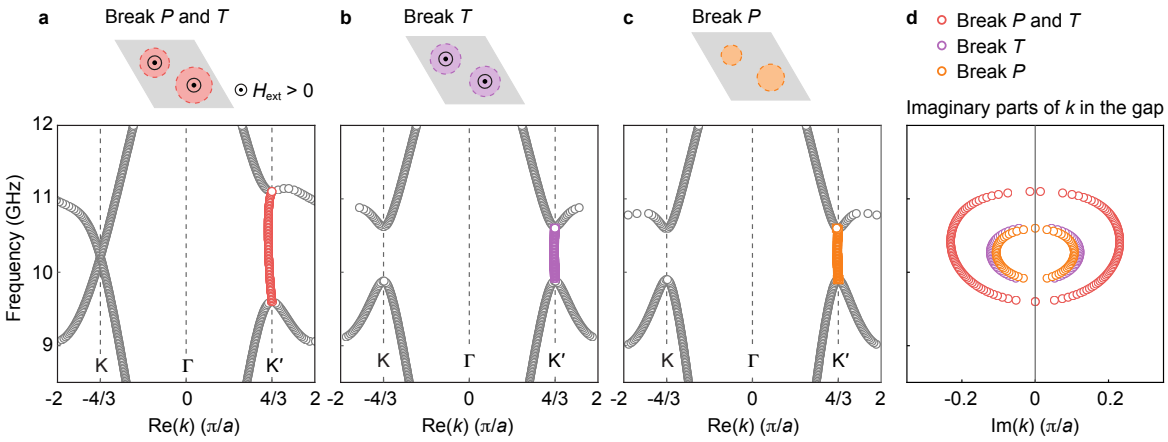

FIG. S7. **The synergistic effect of $\mathcal{T}$ and $\mathcal{P}$ breaking on the valley gap. a-c**, Real parts of the wavenumber from complex-k band diagrams for PCs alongk_y = 0 direction under different symmetry-breaking conditions: (**a**) type-A PVHSM with both $\mathcal{T}$- and $\mathcal{P}$-breakings, (**b**)photonic Chern insulator with $\mathcal{T}$-breaking only, and (**c**)photonic insulator with $\mathcal{P}$-breaking only. **d**, Imaginary parts of wavenumbers for bands (marked by colored circles in **a-c**) located within the band gaps at valley K. Parameters: (**a**), identical to type-A PC in Fig. 2c of the main text. (**b**), YIG cylinder diameters: $d_1 = d_2 = 3.35$ mm, with all other parameters matching **a**. (**c**), YIG cylinder diameters: $d_1 = 2.75$ mm and $d_2 = 3.15$ mm, with no external magnetic field applied.

due to open boundary conditions. The PC parameters used here are identical to those in Figs. S7 b and c, ensuring that the $\mathcal{P}$ or $\mathcal{T}$ symmetry breaking strength in each photonic insulator equals that of the PVHSMs used in the main text (cf. Fig. S8e) and hence the valley gap width in each domain is half that of the PVHSMs.

The band diagram of this interface-state waveguide array (Fig. S8d) closely resembles that of the $|A_4B_4C_4D_4|_1$ photonic highway, confirming that it also provides four alternating one-way channels for light. However, a critical difference emerges: the intra-valley coupling in the conventional interface-state waveguide (signified by the gaps between interface bands ❶,❸ and between ❷,❹ in Fig. S8d) is substantially larger than that in the topological photonic highway (signified by the

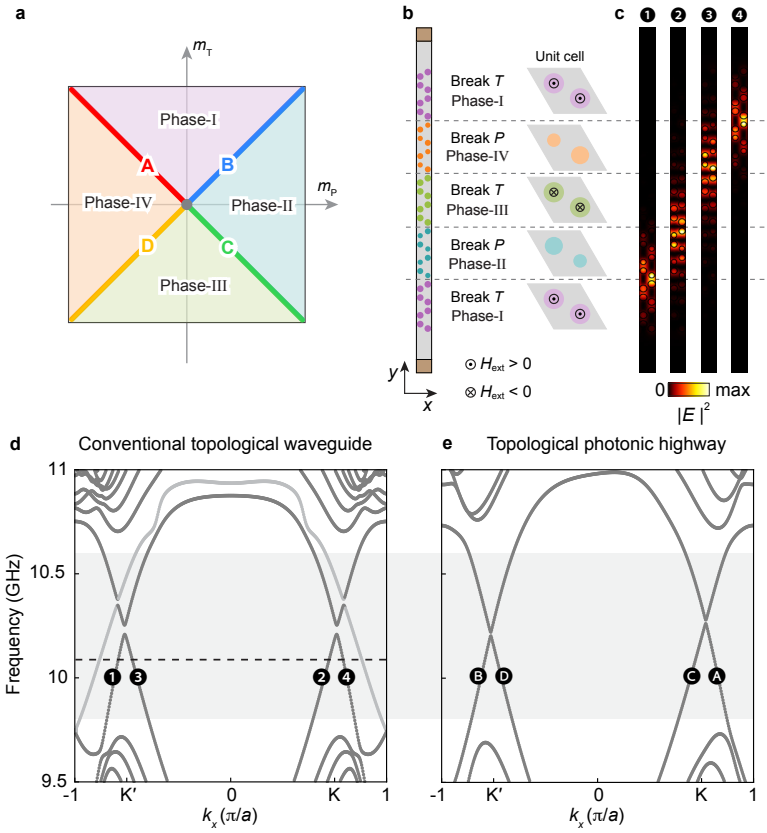

FIG. S8. **Design of a multilane topological interface-state waveguide.** **a**, Phase diagram of the photonic graphene (reproduced from Fig.1c, main text). **b**, Supercell of the multilane topological interface-state waveguide composed of four gapped PCs in phases I to IV in **a**, respectively. The parameters of phase-I PC and phase-IV PC match those in Fig. S7b and Fig. S7c, respectively. Phase-I and Phase-III PCs are time-reversal partners, while Phase-II and Phase-IV PCs are space-inversion partners. **c**,**d**, Projected band structures (**d**) and corresponding topological interface eigenstates (**c**) at 10.1GHz (dashed lines in **d**) for the supercell shown in **b**. **e**, Projected band structures of the topological photonic highway (supercell shown in Extended Data Fig.3d, main text) used in the main text. The lighter gray bands in **d** correspond to the edge states localized at lower and upper outermost boundaries, whose eigenfield modes are not shown in **c**.

gaps between bands A,C and between bands B,D in Fig. S8e). This larger intra-valley gap directly indicates stronger inter-domain crosstalk, which significantly degrades the unidirectional transport performance. To quantitatively demonstrate this effect, we compare the transport performance of these two structures in Fig. S9.

First, we introduce a power attenuation ratio along a waveguide channel to characterize the crosstalk strength during wave transport,

$$\tau(x, f) = \frac{P(x, f)}{P(x_0, f)}, \tag{S23}$$

where

$$P(x, f) = \int_{y_i - W}^{y_i + W} \bar{S}_x(x, y, f)\, \mathrm{d}y \tag{S24}$$

represents the power flux passing through the transverse section centered at (x, y_i) with a transverse width $2W$ (the gray vertical solid line segment in Figs. S9 c-e and h-j). Here, $\bar{S}_x$ denotes the x component of the time-averaged Poynting vector, $W = 4a_y$ is the domain width, and y_i marks the interface (interface waveguide) or domain center (photonic highway). $P(x_0, f)$ represents the power flux at the input position x_0, where $x_0 = 0$ for leftward propagation and $x_0 = 50a$ for rightward propagation.

As shown in Figs. S9a-e, we place a source (blue stars in Figs. S9c,d) at the left side of the interface between domain-I and domain-II to excite state-❶ and a source (red star in Fig. S9e) at the right side of the interface between domain-IV and domain-I to excite state-❹. The right panels of Figs.S9a and b show the power attenuation rates for different interface channels as functions of propagation length and frequencies. Within the one-way propagation frequency window, $\tau \approx 1$ across a large frequency range, indicating negligible energy attenuation during propagation. As exemplified in Fig. S9c, the field profile remains stable throughout the propagation distance at 10.35 GHz. However, near the crossing point of each pair of interface bands at the same valley (near 10.235 GHz), τ exhibits a significant dip, indicating strong inter-domain crosstalk within a considerable frequency range. As illustrated in Fig. S9d, when the field is excited at interface-(I,II), its intensity decreases remarkably along the propagation direction due to crosstalk-induced energy leakage through the backward interface-(III, IV) channel. At the waveguide output ($\Delta x = 50a$), the field becomes nearly invisible (< 0.25) with most energy transferred to interface-(III, IV). Similar behavior occurs near the interface gap at the K-valley, where fields excited at interface-(IV,I) experience enormous energy leakage into the interface-(II,III) channel (as shown in Fig. S9e).

In our topological photonic highway, although intra-valley coupling also induces inter-domain crosstalk, this crosstalk effect is significantly weaker than that in the topological interface waveguides, as shown in Figs. S9f-j. The field distributions in Figs. S9 i and j exhibit that the power

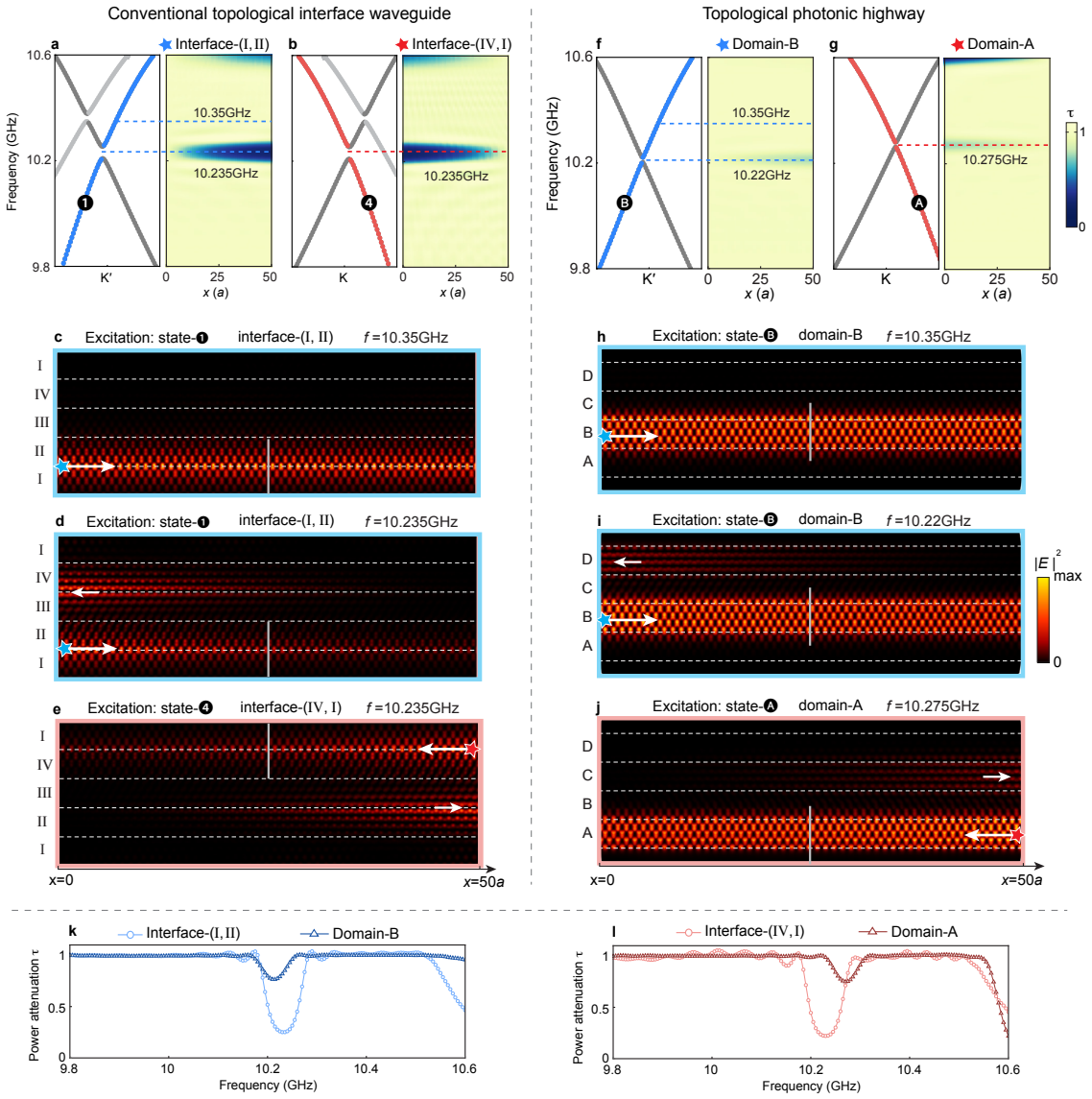

FIG. S9. **Comparison of intra-valley inter-domain crosstalks in (a-e) topological interface-state waveguide and in (f-j) topological photonic highway.** **a**,**b**, Left panel: zoom-in of band diagrams (shaded region in Fig. S8d) near the (**a**) K′ valley and (**b**) K valley of the multilane topological interface waveguide in Fig. S8b. Right panel: power attenuations, $\tau(x,f) = P(x,f)/P(x_0,f)$, for (**a**) the rightward interface state (blue) between domains I and II (❶ in **a**) and for (**b**) the leftward interface state (red) between domains IV and I (❹ in **b**). **c**-**e**, Propagation of interface-(I, II) states and interface-(IV, I) state, corresponding to the dashed lines in **a** and **b**. **f**,**g**, Left panel: zoom-in of band diagrams (shaded region in Fig. S8e) near the (**f**) K′ valley and (**g**) K valley of the topological photonic highway. Right panel: power attenuation, $\tau(x,f)$, for (**f**) the rightward domain-B state(blue) and for (**g**) leftward domain-A state(red). **h**-**j**, Propagation of domain-A state and domain-B state in the topological photonic highway, corresponding to the dashed lines in **f** and **g**. **k**,**l**, Comparison of power attenuation at output ports: (**k**) $\tau(x = 50a, f)$ for interface-(I,II) state in **a** versus domain-B state in **f**; (**l**) $\tau(x = 0, f)$ for interface-(IV,I) state in **b** versus domain-A state in **g**.

attenuations in the topological photonic highways are almost unnoticeable even at the frequencies exhibiting the strongest crosstalk. Figures S9k,j provide direct quantitative evidence of this contrast. After propagating through 50 unit cells, the power attenuation dip in interface waveguides exhibits both significantly greater width and depth compared to that in the topological photonic highway—a clear demonstration of superior crosstalk suppression in our design.

In conclusion, the shorter mode localization lengths in topological photonic highways result in significantly reduced inter-domain crosstalk between intra-valley intersecting modes, compared to conventional topological interface waveguide arrays with identical symmetry-breaking strength and domain widths. Since $\mathcal{T}$-breaking strength is limited by magneto-optical effect, PVHSMs enable larger bandgaps without stronger magneto-optic response, allowing reduced domain widths and higher spatial channel density than conventional topological interface waveguides. If we use conventional edge transport, the lanes have to be wider to suppress crosstalk among the lanes and hence the spatial use is less effective.

B. Comparison between topological photonic highways and high Chern number photonic crystals

High-Chern-number photonic crystals [1, 2] can support multiple modes in a single transmission channel (edge or interface of photonic Chern insulators), theoretically enabling high information capacity per unit area. However, this density comes with practical challenges. Our topological photonic highways, in contrast, prioritize spatial channel separability, which yields three key benefits:

1. **Complexity in multi-channel signal manipulation.** In high-Chern-number photonic crystals, multiple modes share a single interface channel, making space-division multiplexing technically challenging. This becomes particularly challenging when numerous interface modes that lack distinguishing symmetry properties are all physically squeezed in the same channel, making the design of effective multiplexers and demultiplexers extremely complicated. In contrast, our topological photonic highways employ spatially distinct waveguide regions for different information channels, enabling straightforward mode selection through spatial addressing.

2. **Reduced crosstalk due to spatial separation of modes.** Compared to the multimode transmission supported by high-Chern-number photonic crystals, where modes propagate along a shared interface and are prone to mode mixing from perturbations or bends, our designed multi-lane waveguides feature modes that are spatially separated across distinct regions. Theoretically, this spatial separation should result in lower crosstalk in the presence of local disorders or sharp bends, enhancing signal integrity and overall information capacity.

3. **Trade-off between mode number and bandwidth.** For high Chern number photonic crystals, higher Chern numbers typically correspond to narrower bandgaps. Recent studies based on quantum geometry have demonstrated that the Chern number imposes an upper bound on the bandgap width [3]. While increasing the Chern number enables more modes, it necessarily reduces the channels bandwidth. Conversely, in our topological photonic highways, the unidirectional propagation bandwidth is determined solely by individual PVHSM waveguide width, showing no dependence on the systems total number of modes.

Therefore, while both approaches can achieve high information capacity, our design offers a more scalable and practically robust pathway for multi-channel information processing.

C. Comparison between topological photonic highways and traditional optical isolation techniques

Traditional optical isolation techniques can also achieve unidirectional transport. Below, we provide comparisons between two representative optical isolation techniques [4] and our proposed topological photonic highways:

1. **Faraday rotation-based isolators.** Conventional Faraday isolators rely on non-reciprocal polarization rotation in magneto-optical media, requiring additional polarizers at the terminals of magneto-optical media, which results in different input and output polarization states. In contrast, our system achieves isolation while maintaining polarization states. Faraday isolators require specific optical lengths for optimal isolation, whereas our topological photonic highways can function effectively at almost any length. Since the Faraday effect employs in-plane magnetic fields, light propagation is restricted to straight paths. Conversely, topological photonic highways maintain ideal isolation even under severe bending and deformation. Finally, traditional Faraday isolators present significant challenges for integration, as they are typically bulky 3D components. Our planar 2D design is inherently more scalable and suitable for high-density photonic circuits.

2. **Nonreciprocal phase-shifting isolators.** These devices achieve isolation through nonreciprocal phase shifts in Mach-Zehnder interferometers or ring resonators. However, they require precise path length control for interference effects and occupy substantial chip area, limiting their integration density. In contrast, topological photonic highways operate independently of path length constraints and enable ultra-compact multi-channel integration.

In general, comparing to traditional isolation techniques, our method leverages intrinsic topological nature for nonreciprocal transport, providing global protection embedded in the band struc-

ture, independent of local perturbations. It offers complementary robustness against manufacturing variations and environmental factors.

S4. Multi-lane unidirectional focusing and defocusing arrays

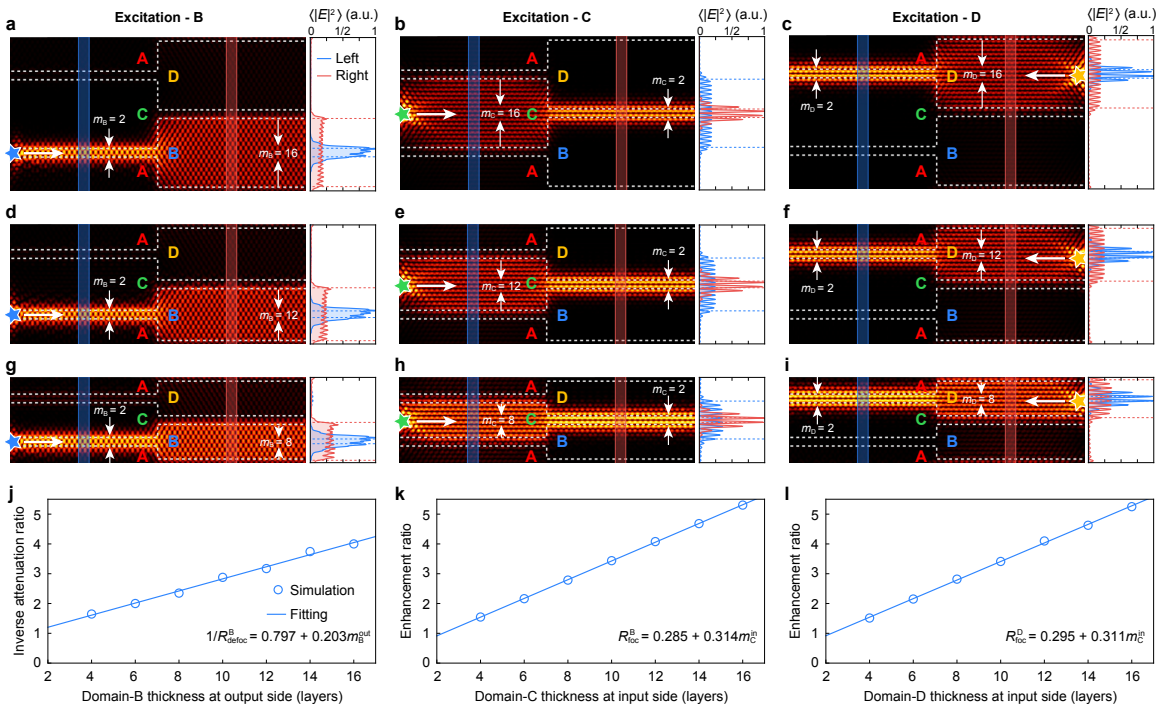

FIG. S10. **Multi-lane unidirectional focusing and defocusing arrays.** **a**,**d**,**g**, Left-to-right unidirectional defocusing in domain B. **b**,**e**,**h**, Left-to-right unidirectional focusing in domain C. **c**,**f**,**i**, Right-to-left unidirectional focusing in domain D. Configurations: (**a**,**b**,**c**) Left side $|A_{16}B_2C_{16}D_2|$, right side $|A_2B_{16}C_2D_{16}|$; (**d**,**e**,**f**) Left side $|A_{12}B_2C_{12}D_2|$, right side $|A_2B_{12}C_2D_{12}|$; (**g**,**h**,**i**) Left side $|A_8B_2C_8D_2|$, right side $|A_2B_8C_2D_8|$. Periodic boundary conditions connect the upper and lower boundaries in each configuration. **j**, Inverse of intensity attenuation ratio in domain B, $1/R^{\mathrm{B}}_{\mathrm{defoc}}$, versus domain-B thickness at output (right) side. **k**, Intensity enhancement ratio in domain C, $R^{\mathrm{C}}_{\mathrm{foc}}$, versus domain-C thickness at input (left) side. **l**, Intensity enhancement ratio in domain D, $R^{\mathrm{D}}_{\mathrm{foc}}$, versus domain-D thickness at input (right) side. The operating frequency is 10.25 GHz.

A key application of topological photonic highways is multi-channel field morphing in ultra-compact spaces, such as dense focusing and defocusing arrays. To quantitatively characterize the focusing and defocusing performance of the topological photonic highways, we designed a structure as shown in Fig. S10, where four domains are alternately arranged into wide and narrow waveguides, achieving densely packed unidirectional focusing and defocusing arrays through abrupt width expansions and contractions.

We analyze three adjacent domains: domain B supports left-to-right unidirectional defocusing

(Fig. S10a,d,g), domain C enables left-to-right unidirectional focusing (Fig. S10b,e,h), and domain D supports right-to-left focusing (Fig. S10c,f,i). The layer configuration varies from 4 to 16 layers on the wide side of each region, while maintaining a constant two-layer structure ($m = 2$) on the narrow side. As demonstrated in Figs. S10a-i, unidirectional focusing and defocusing are perfectly achieved across all configurations with negligible inter-domain crosstalk. In both left and right parts, we select regions of uniform field distribution (indicated by blue and red shaded strips with a width of $w = 2a$) distant from both the source and width-transition interfaces, and calculate the field intensities averaged along the x-direction:

$$\left\langle |E|^2 \right\rangle_{L|R}(y) = \frac{1}{w}\int_{x_{L|R}-w/2}^{x_{L|R}+w/2} dx\,|E_z(x,y)|^2 \tag{S25}$$

where $x_{L|R}$ denote the x-coordinates at the center of the left- and right-side strips, respectively. The resulting transverse intensity distributions before and after focusing (defocusing) are displayed in the right panel of each subfigure. Based on the ratio of peak transverse field intensities before and after focusing (defocusing), we define the intensity attenuation ratio for defocusing and the intensity enhancement ratio for focusing processes in the three domains, respectively:

$$R^{\mathrm{B}}_{\mathrm{defoc}} = \frac{\max\left[\left\langle |E|^2 \right\rangle_R(y)\right]}{\max\left[\left\langle |E|^2 \right\rangle_L(y)\right]}, \quad R^{\mathrm{C}}_{\mathrm{foc}} = \frac{\max\left[\left\langle |E|^2 \right\rangle_R(y)\right]}{\max\left[\left\langle |E|^2 \right\rangle_L(y)\right]}, \quad R^{\mathrm{D}}_{\mathrm{foc}} = \frac{\max\left[\left\langle |E|^2 \right\rangle_L(y)\right]}{\max\left[\left\langle |E|^2 \right\rangle_R(y)\right]}. \tag{S26}$$

The inverse intensity attenuation ratio for domain B and the intensity enhancement ratios for domains C and D are presented in Figs. S10j-l, respectively. Both $1/R^{\mathrm{B}}_{\mathrm{defoc}}$ and $R^{\mathrm{C}}_{\mathrm{foc}}$, $R^{\mathrm{D}}_{\mathrm{foc}}$ exhibit linear growth with increasing thickness of the wider side. Through linear fitting, we obtained the linear coefficients for $1/R^{\mathrm{B}}_{\mathrm{defoc}}$ and $R^{\mathrm{C}}_{\mathrm{foc}}$, $R^{\mathrm{D}}_{\mathrm{foc}}$ with respect to the layer number variation on the wider side.

This dense waveguide architecture of alternating focusing and defocusing arrays have two fundamental constraints. First, narrow sections must maintain sufficient width for electromagnetic isolation, as reduction to a single layer would induce significant inter-region crosstalk. Second, the inverse relationship between waveguide thickness and single-mode one-way bandwidth limits the maximum width of wide sections, thereby constraining the achievable intensity modulation ratios in focusing and defocusing processes.

S5. Experimental setup and measurement details

A. Experimental setup for the straight ABCD-configured waveguide

The photograph of the ABCD-configured waveguide sample used for measuring the four one-way waveguide modes (Fig.2i of main text) and the alternating unidirectional waveguiding properties

(Fig.3c of main text) are shown in Fig. S11a. The white dielectric foam for stabilizing the YIG rods has a relative permittivity close to air (≈ 1). The carbon powder-infused black foam functions as an electromagnetic absorber to terminate the multi-lane waveguides, which can prevent unwanted reflections (see Section S5 B for details).

Colored stars in Fig. S11b indicate excitation positions in different domains. Black dots along longitudinal lines (P_A, P_B, P_C, P_D) mark the probing positions for the band structure of waveguide modes shown in Fig.2i. Black dots along transverse lines (P_L and P_R) mark probing positions for the field distributions presented in Fig. 3c.

B. Effect of absorbing termination on wave propagation

Although the waves propagate unidirectionally in each waveguide domain, improper termination may cause reflections at the waveguide ends that propagate back into adjacent channels. To prevent these unwanted reflections, we terminate all input and output ports with absorbing foam in both simulations and experiments (as exemplified in Fig. S12), effectively absorbing outgoing waves. Figure S12 demonstrates this approachs effectiveness in bent waveguides, the electromagnetic field excited in domain B is well-absorbed in the termination region, confirming minimal reflection at the ports.

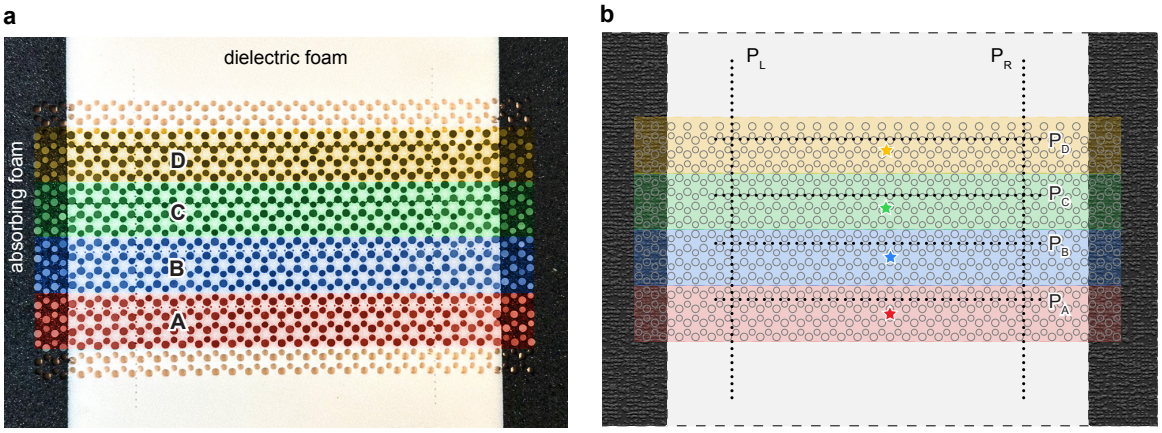

FIG. S11. **Measurement setup for the straight ABCD-configured waveguide. a**, Photograph of the $|A_4B_4C_4D_4|_1$ configured waveguide. The carbon powder-infused black foam functions as an electromagnetic absorber with a dielectric constant of 1.87 (real part) and loss tangent of 0.36 near 10 GHz. **b**, Schematic showing the excitation (colored stars) and probing positions (black dots).

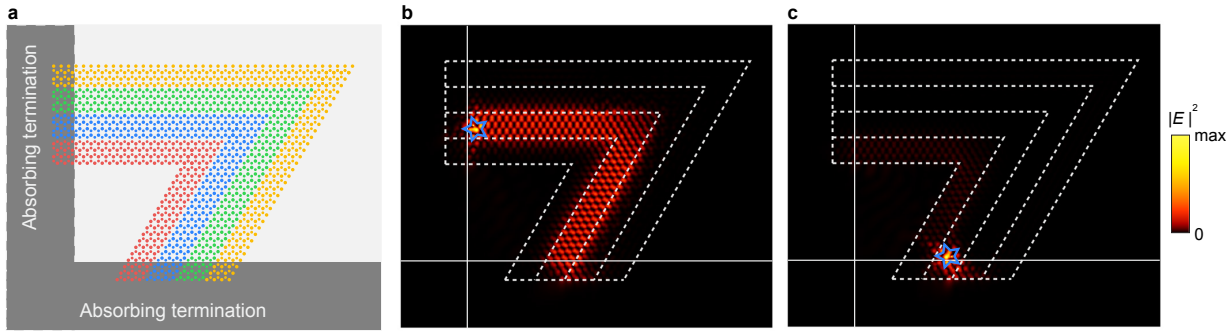

FIG. S12. **Effect of absorbing termination on wave propagation.** **a**, Schematic of simulation setup for a topological multilane highway with a 120° bend: the YIG rods at the left and bottom ports are embedded in absorbing foams with a dielectric constant of 1.87 (real part) and loss tangent of 0.36. **b**,**c**, Simulated field intensity distributions at 10.35 GHz for domain-B excitations at left port (**b**) and bottom port (**c**) with source positions marked by blue stars.

C. Transmission measurement of a sharply bent topological photonic highway

Experimental limitations in excitation and measurement methods prevent direct measurement of the S-matrix defined in the previous section S2. Instead, we use the T-matrix to qualitatively represent relative transmission field strengths under different excitations, indicating the dominant transmission channels for electromagnetic waves (see Methods). As shown in Fig. S13, the simulation and experimental results agree well in the frequency window of domain-selective one-way propagation, validating the reliability of our measurements.

S6. Designs of topological photonic highways for Terahertz and optical frequencies

A. Terahertz-regime design using magnetized semiconductor materials

As documented in the literature [5–7], narrow-gap semiconductor materials, such as Indium antimonide (InSb) and Indium arsenide (InAs), exhibit strong magneto-optical effects in the Terahertz regime and have established fabrication processes for integrated photonics. Here, as an illustrative example, we present a three-dimensional (3D) design using InSb as the substrate material, with experimentally feasible parameters for Terahertz PVHSMs.

Figure S14a illustrates the unit cell of the designed photonic chip, where an etched silicon photonic crystal is attached on top of an InSb slab. In the presence of an external magnetic field

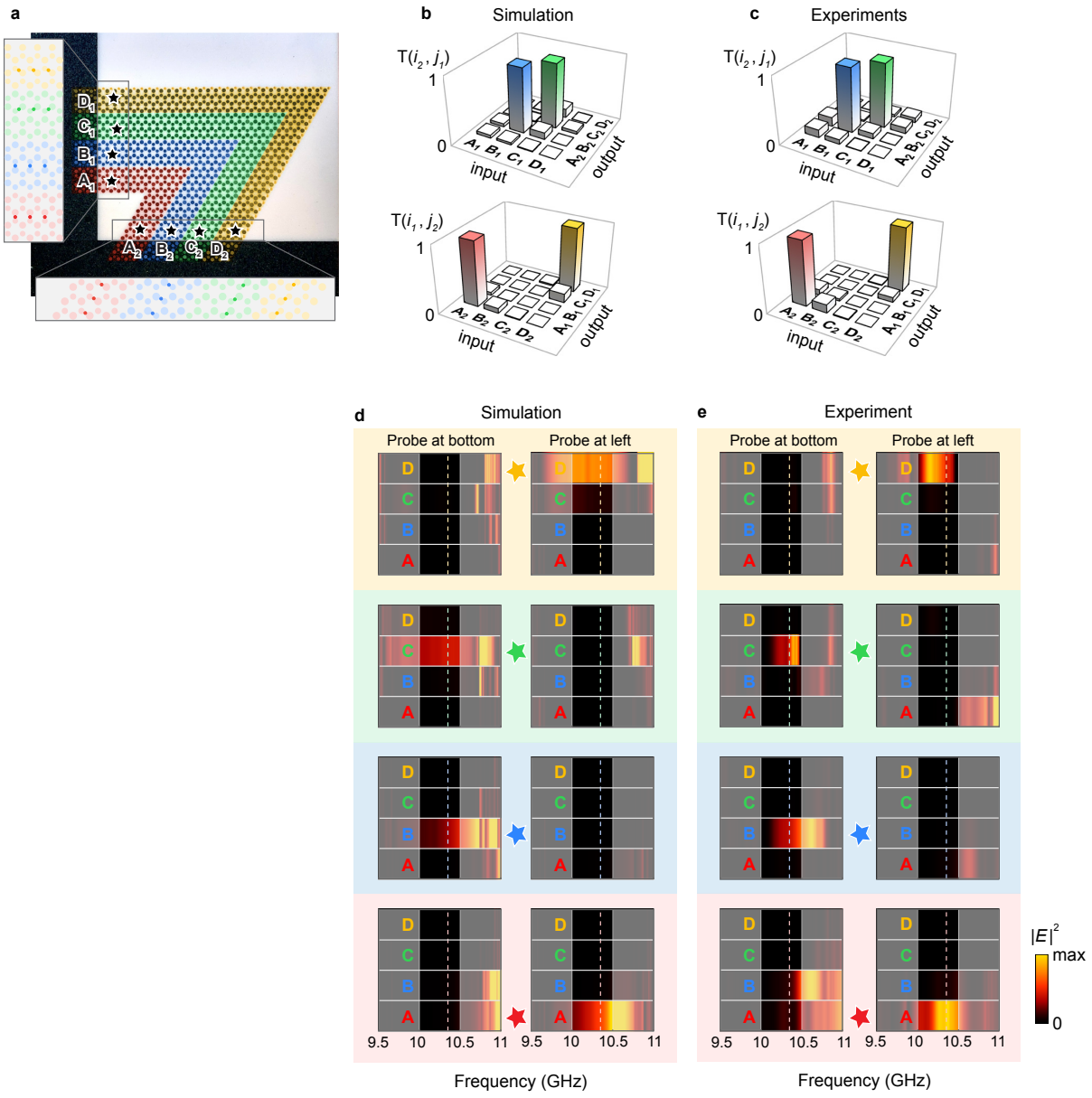

FIG. S13. **Transmission measurement of a sharply bent topological photonic highway.** **a**, Experimental setup of an $|A_4B_4C_4D_4|_1$ configured waveguide with a 120° sharp bend. Black stars indicate excitation port positions in different domains: $A_1 - D_1$ for left ports and $A_2 - D_2$ for bottom ports. Insets show probe positions in waveguides A, B, C, and D, marked by red, blue, green, and yellow dots, respectively. **b**,**c**, Normalized T-matrix elements for simulated (**b**) and experimentally measured (**c**) transmissions at 10.35 GHz: left-to-bottom transmission $T(i_2, j_1)$ (upper panel) and bottom-to-left transmission $T(i_1, j_2)$ (lower panel). **d**,**e**, Simulated (**d**) and measured (**e**) average field intensities in different waveguides under various excitations (marked by colored stars). Left panels: excitation at left ports, probing at bottom ports. Right panels: excitation at bottom ports, probing at left ports. Unshaded regions indicate the frequency window for alternating unidirectional waveguiding. Dashed lines mark the 10.35 GHz operating frequency.

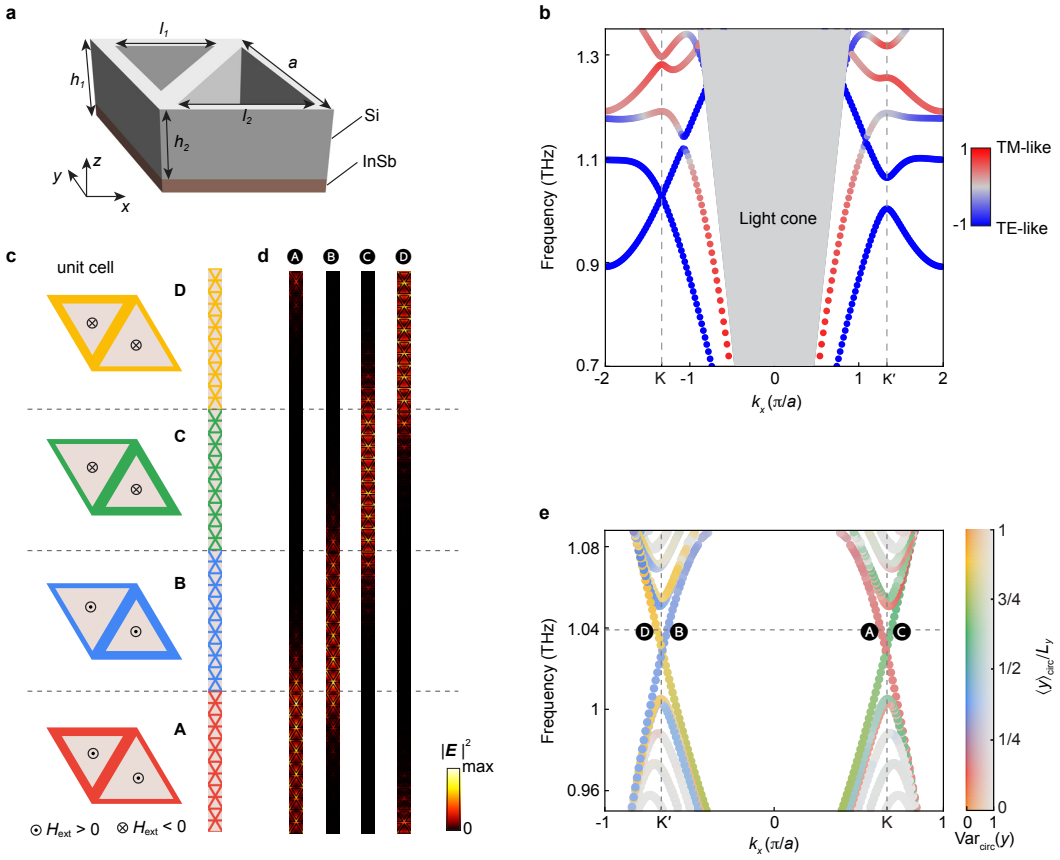

FIG. S14. **Design of a topological photonic highway at Terahertz frequencies.** **a**, Unit cell of a quasi-2D PVHSM for TE-like modes (H_z dominant), comprising silicon with triangular holes ($\varepsilon = 12$, $= 1$) on a magnetically biased InSb slab. Geometric parameters: $a = 100\,\mu$m $l_1 = 0.65a$, $l_2 = 0.8a$, $h_1 = 0.5a$, $h_2 = 0.45a$. **b**, Band structure of the photonic crystal in **a** along $k_y = 0$ with the colors indicating the ratio $\langle |E_z|^2 - |\eta_0 H_z|^2 \rangle_{z=z_0} / \langle |E_z|^2 + |\eta_0 H_z|^2 \rangle_{z=z_0}$ (η_0 denotes the vacuum impedance) averaged at the vertical middle plane of the silicon layer, $z = z_0$, characterizing the relative strength of TM-like and TE-like components. **c**, Unit cells (top view) of four PVHSM types (A-D) and resulting supercell of a 12-layer-per-domain topological photonic highway. **d**, Eigenfield distributions (on the middle plane of the silicon layer) of domain-selective one-way modes near 1.04 THz (labeled in e). **e**, Supercell band structure with colors/saturations representing transverse intensity centroid $\langle y \rangle_{\text{circ}}$ and spread $\text{Var}_{\text{circ}}(y)$. Leaky modes with low Q factors inside the light cone have been filtered out.

$\mathbf{B}_0 = B_0 \hat{\mathbf{z}}$ InSb's relative permittivity becomes gyroelectric [5]:

$$\overleftrightarrow{\varepsilon}_r(\omega) = \begin{pmatrix} \varepsilon_d & i\varepsilon_t & 0 \\ -i\varepsilon_t & \varepsilon_d & 0 \\ 0 & 0 & \varepsilon_z \end{pmatrix}, \tag{S27}$$

$$\varepsilon_d(\omega) = \varepsilon_\infty \left(1 - \frac{\omega_p^2(\omega + i\gamma)}{\omega((\omega + i\gamma)^2 - \omega_c^2)}\right), \quad \varepsilon_t(\omega) = \frac{\varepsilon_\infty \omega_p^2 \omega_c}{\omega\left((\omega + i\gamma)^2 - \omega_c^2\right)}, \quad \varepsilon_z(\omega) = \varepsilon_\infty \left(1 - \frac{\omega_p^2}{\omega^2 + i\gamma\omega}\right), \tag{S28}$$

where the electron cyclotron frequency $\omega_c = eB_0/m^*$ with $m^* = 0.015m_0$ being the effective mass of electron in InSb, and e and m_0 being the electric charge and electron mass, respectively. At an external magnetic field strength of $B_0 = 0.47\,\mathrm{T}$, the cyclotron frequency takes the value of $\omega_c/2\pi = 0.88\,\mathrm{THz}$. We adopt other material parameters from Ref. [5], measured at a low temperature of $T = 50\,\mathrm{K}$: high-frequency dielectric constant $\varepsilon_\infty = 16$, plasma frequency $\omega_p/2\pi = 0.31\,\mathrm{THz}$, and damping factor $\gamma/2\pi = 0.03\,\mathrm{THz}$. Taking these parameters, we obtain the relative permittivity of InSb at the operating frequency $f_0 = \omega_0/2\pi = 1.03\,\mathrm{THz}$,

$$\overleftrightarrow{\varepsilon}_r(\omega_0) = \begin{pmatrix} 10.9 + 0.9i & i(4.3 - 0.9i) & 0 \\ i(4.3 - 0.9i) & 10.9 + 0.9i & 0 \\ 0 & 0 & 14.6 + 0.04i \end{pmatrix}. \tag{S29}$$

In computing the band structure, we assumed a constant permittivity as specified in Eq. (S29) for simplicity.

Here, we focus on TE-like modes (blue curves in Fig. S14b) only. Around $f_0 = 1.03\,\mathrm{THz}$, an accidental Dirac point forms at K valley while the gap at K′ valley remains open, resulting in a photonic valley half-semimetal (PVHSM). By alternating the sizes of the triangular holes and the magnetization directions, we obtain four inequivalent PVHSMs, similar to those in the main text. Arranging the four PVHSMs periodically in the sequence A, B, C, D, as illustrated in the supercell in Fig. S14c, a topological photonic multi-lane highway is achieved in the Terahertz regime. The band structure and eignfields in Fig. S14d,e reveals domain-selective chiral single-mode characteristics within a frequency window near the Dirac frequency.

B. Optical frequency design using time-reversal symmetric materials

In the near-infrared regime [8, 9], the relatively weak gyrotropic response significantly constrains experimental feasibility. To address this limitation, we extend the PVHSM concept to nonmagnetic multi-valley half-semimetals, enabling the design of a topological photonic highway without breaking time reversal symmetry (TRS).

TRS constrains the bandgaps at time-reversal paired valleys to be identical, necessitating at least two independent pairs of valleys to realize a PVHSM. We achieve this using a prototypical dielectric (Silicon) photonic crystal with C_{4v} symmetry (Fig. S15a), where mirror symmetries along x and y directions protect the formation of two pairs of time-reversal-partner Dirac points (X_1,X_2 and Y_1,Y_2) on distinct Brillouin zone boundaries (Fig. S15b), establishing two independently controllable valley pairs (totaling four valleys). As shown in the Fig. S15c-f, breaking the mirror symmetry M_x (or M_y) while preserving the other one can gap the two valleys (X_1,X_2) along XM (or Y_1,Y_2 along YM), leaving the Dirac points (Y_1,Y_2) along YM (or X_1,X_2 along XM)

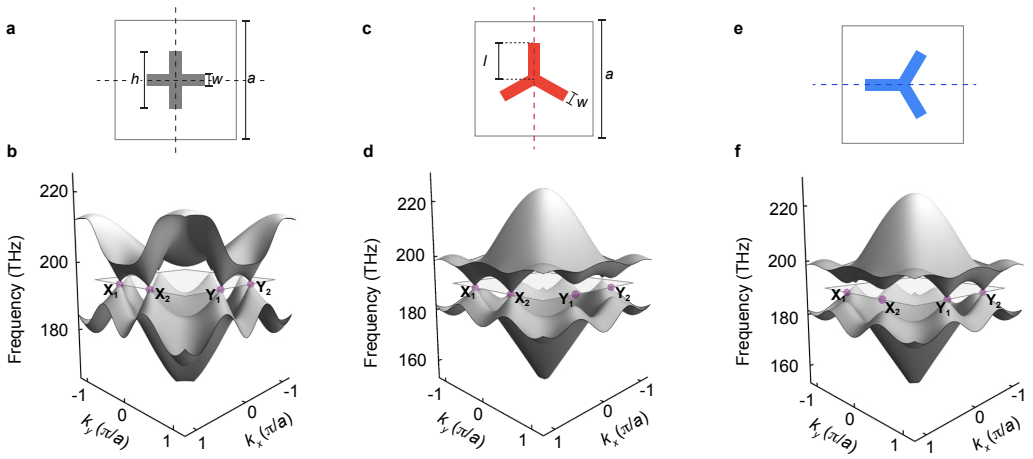

FIG. S15. **Photonic multi-valley half-semimetals. a-f**, Unit cells (**a**,**c**,**e**) and TM band structures (**b**,**d**,**f**) of silicon photonic crystals exhibiting (**a**,**b**) C_{4v} point-group symmetry, (**c**,**d**) mirror-x symmetry, and (**e**,**f**) mirror-y symmetry. The dashed lines indicate the mirror planes. The cross in (**a**) and three-arm junction structures in (**c**,**e**) are composed of silicon (ε = 12, μ = 1). Geometric parameters: a = 1180 nm, $w = 0.1a$, $h = 0.48a$, $l = 0.31a$.

intact. This configuration realizes a photonic multi-valley half-semimetal, where one pair of time-reversal-partner valleys exhibits insulating behavior while the other pair maintains semimetallic characteristics.

Starting with the structure in Fig. S15c (type-A), we generate three additional photonic multi-valley half-semimetals (types B, C, and D) through successive 90° counterclockwise rotations as illustrated in Fig. S16a-d. The periodic arrangement of these structures creates a time-reversal-symmetric topological photonic multi-lane highway. The valley pairs (X_1,X_2 and Y_1,Y_2) exhibit alternating bandgap opening and closing between adjacent domains, while next-nearest-neighbor domains display opposite valley Chern number distributions. This configuration enables domain-selective valley-momentum-locked wave propagation, confirmed by supercell band structure (Fig. S16g) near 190 THz (band colors indicate mode locations). The coincident projection of valleys X_1 and X_2 results in nearly degenerate guided bands in domains A and C (shown as red-green dashed lines).

In Fig. S17, the numerical simulations demonstrate valley-momentum locked propagation in each waveguiding domain. We performed 2D discrete Fourier transformation of the excited fields over the entire displayed area: $\tilde{\mathcal{E}}(\mathbf{k}) = \sum_{\mathbf{r}} e^{-i\mathbf{k}\cdot\mathbf{r}} E(\mathbf{r})$. By mapping all plane-wave components in the discrete Fourier spectrum to the first Brillouin zone (BZ), we determined the effective Bloch-wave intensity distribution in the excited field:

$$\left|\tilde{E}(\mathbf{k})\right|^2 = \sum_{\mathbf{K}} \left|\tilde{\mathcal{E}}(\mathbf{k}+\mathbf{K})\right|^2, \quad \mathbf{k} \in \text{ first BZ}, \tag{S30}$$

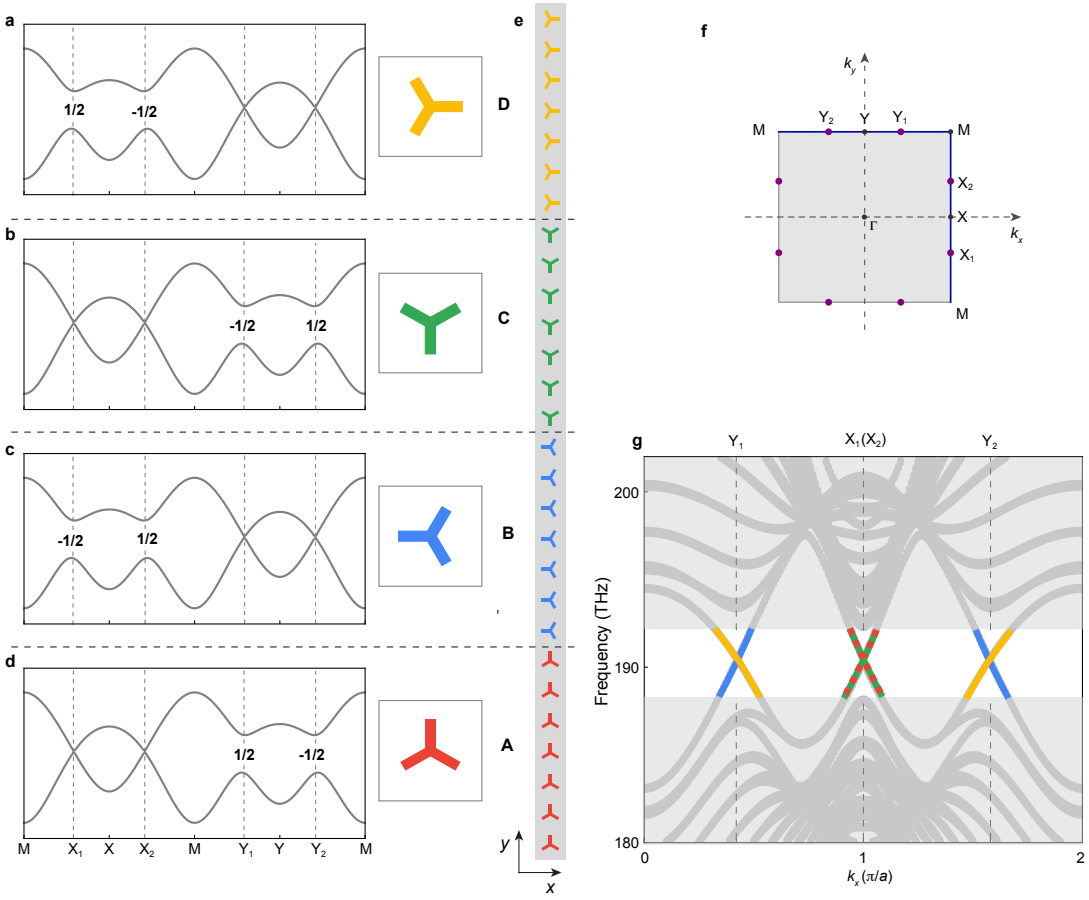

FIG. S16. **Time-reversal-symmetric topological photonic highway. a-d**, Band structures along Brillouin zone boundaries (blue lines in **f**) for four types of photonic multi-valley half-semimetals (A, B, C, and D) with corresponding unit cells shown in right panels. Valley-Chern numbers (approximate to 1/2 or −1/2) of the lower band are indicated at each valley. **e**, Supercell of the topological photonic highway (7 layers per domain), with a periodic boundary condition connecting the upper and lower boundaries. **f**, Square-lattice Brillouin zone showing locations of two time-reversal-partner valley pairs (X_1,X_2 and Y_1,Y_2). **g**, Supercell band structure displaying valley-polarized waveguide modes in domains B (blue lines) and D (yellow lines), and nearly degenerate waveguide modes in domains A and C (red-green dashed lines).

where **K** are reciprocal lattice vectors covered by the discrete Fourier spectrum. The lower panels in Figs. S17a-h exhibit the obtained Bloch spectra of the excited fields, where the spectra in the higher-order BZs are just the repetitions of those in the first BZ. The Bloch spectra reveal that each domain supports propagation only at a specific time-reversal-partner valley pair, with different propagation directions exciting distinct valleys. Figure S18 further validates the robust sharp-turn propagation of valley-locked modes, showing negligible inter-domain scattering even at

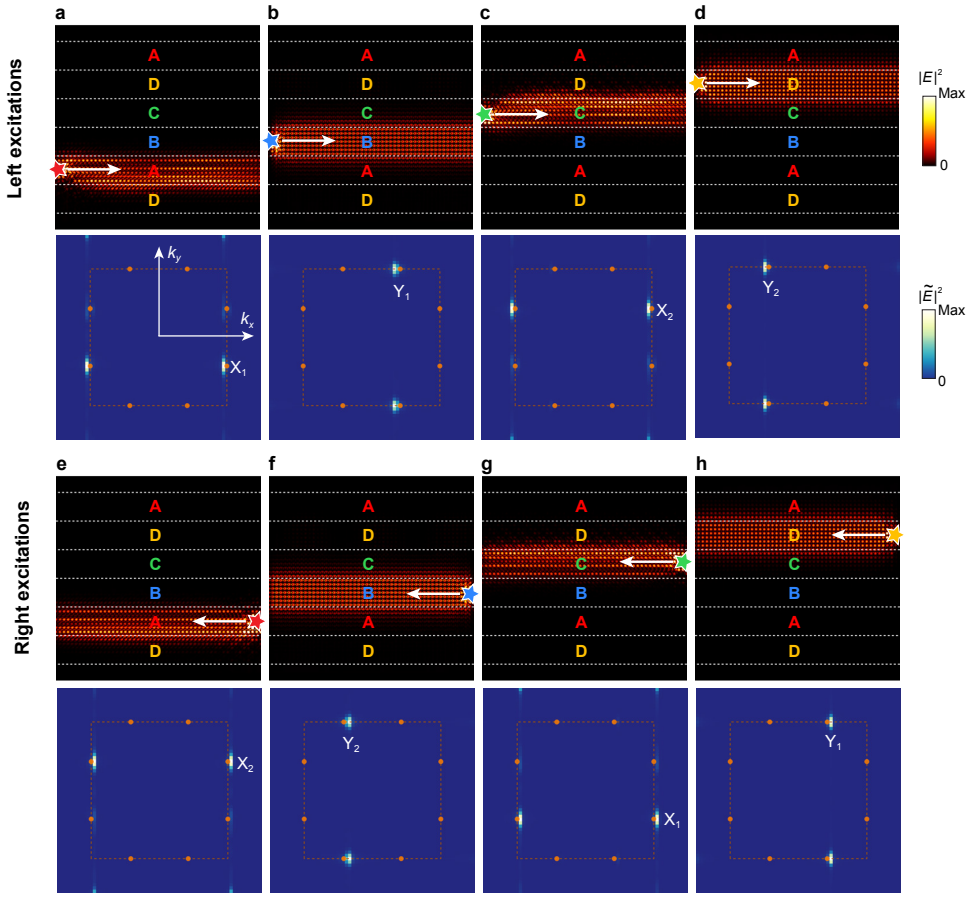

FIG. S17. **Valley-polarized waveguiding in time-reversal-symmetric topological photonic highway. a-h**, Simulated field intensity distributions (upper panels) and the corresponding momentum-space Bloch spectra (lower panels) at 190 THz for domain-specific excitations at left ports (**a-d**) and right ports (**e-h**), with source positions marked by stars.

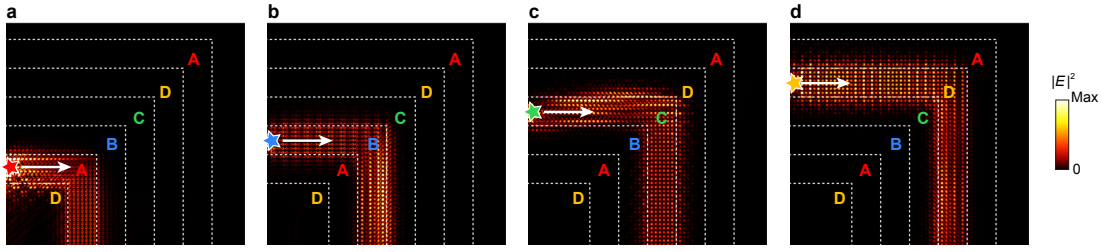

FIG. S18. **Demonstration of robust waveguiding in a sharply bent time-reversal-symmetric topological photonic highway. a-d**, Simulated field intensity distributions at 190 THz for domain-specific excitations at left ports, with source positions marked by stars.

sharp bends, thus confirming the robustness of the propagation.

---

[1] S. A. Skirlo, L. Lu, and M. Soljačić, Multimode One-Way Waveguides of Large Chern Numbers, Phys. Rev. Lett. **113**, 113904 (2014).

[2] S. A. Skirlo, L. Lu, Y. Igarashi, Q. Yan, J. Joannopoulos, and M. Soljačić, Experimental Observation of Large Chern Numbers in Photonic Crystals, Phys. Rev. Lett. **115**, 253901 (2015).

[3] Y. Onishi and L. Fu, Fundamental bound on topological gap, Phys. Rev. X **14**, 011052 (2024).

[4] K. Srinivasan and B. J. H. Stadler, Review of integrated magneto-optical isolators with rare-earth iron garnets for polarization diverse and magnet-free isolation in silicon photonics, Opt. Mater. Express **12**, 697 (2022).

[5] D. Wang, B. Yang, W. Gao, H. Jia, Q. Yang, X. Chen, M. Wei, C. Liu, M. Navarro-Cía, J. Han, W. Zhang, and S. Zhang, Photonic Weyl points due to broken time-reversal symmetry in magnetized semiconductor, Nat. Phys. **15**, 1150 (2019).

[6] R. Jia, T. C. Tan, S. S. Mishra, W. Wang, Y. J. Tan, and R. Singh, On-Chip Active Non-Reciprocal Topological Photonics, Adv. Mater. **37**, 2501711 (2025).

[7] M. Liu, S. Xia, W. Wan, J. Qin, H. Li, C. Zhao, L. Bi, and C.-W. Qiu, Broadband mid-infrared non-reciprocal absorption using magnetized gradient epsilon-near-zero thin films, Nat. Matter. **22**, 1196 (2023).

[8] B. Bahari, A. Ndao, F. Vallini, A. E. Amili, Y. Fainman, and B. Kanté, Nonreciprocal lasing in topological cavities of arbitrary geometries, Science **358**, 636 (2017).

[9] B. Bahari, L. Hsu, S. H. Pan, D. Preece, A. Ndao, A. El Amili, Y. Fainman, and B. Kanté, Photonic quantum Hall effect and multiplexed light sources of large orbital angular momenta, Nat. Phys. **17**, 700 (2021).